SPECTROSCOPIC AND LASER PROPERTIES OF Nd:BMAG

By

MICHAEL J. FERRY

Bachelor of Arts

Wake Forest University

Winston-Salem, North Carolina

1985

Submitted to the Faculty of the
Graduate College of the
Oklahoma State University
in partial fulfillment of
the requirements for
the Degree of
MASTER OF SCIENCE
December, 1989

SPECTROSCOPIC AND LASER PROPERTIES
OF Nd:BMAG

Thesis Approved:

Richard C. Powell
Thesis Adviser

Bruce J. Ackerson

Donna Kay Bandy

Norman N. Durham
Dean of the Graduate College

ACKNOWLEDGMENTS

I wish to express my gratitude to all of the people responsible for helping me during my studies at Oklahoma State University. I want to particularly thank my thesis advisor, Dr. Richard C. Powell, for the opportunity of working in his lab and for his guidance and patience. I also wish to thank the other members of my committee, Dr. Donna K. Bandy and Dr. Bruce J. Ackerson for encouragement and constructive criticism.

Special thanks go to Mike L. Kliewer and Dr. Roger J. Reeves for sound advice in the lab and intelligent feedback. Thanks also to Dr. Edward R. Behrens for his help in the word processing of this thesis.

Finally, I would like to deeply thank my parents for their support, encouragement, and understanding throughout graduate school.

Financial support was provided by the U. S. Army Research Office. Samples for this work were provided by Dr. Toomas H. Allik of the Science Applications International Corporation, McLean, VA.

TABLE OF CONTENTS

LIST OF TABLES

LIST OF FIGURES

Figure Page

CHAPTER I

SITE SELECTIVE SPECTROSCOPY

Experiment

Site-selective spectroscopy in Nd:$Ba_2MgGe_2O_7$ (Nd:BMAG) was performed using a Molectron UV-14 nitrogren laser to pump a Molectron DL-II dye laser. Such a system achieves tunable pulses of 10 ns duration, less than half an angstrom in pulsewidth, and pulse energy of 100 mJ. The dyes used were Coumarin-440 and Rhodimine-590 in ethanol, with approximate tuning ranges of 420-460 nm and 570-600 nm.

The sample measured $0.56 \times 0.825 \times 1.02$ cm^3, with the long axis parallel to the $\vec{C}$-axis of the host. The approximate Nd^{3+} ion concentration was 2 molar percent or 1×10^{20} $\frac{ions}{cm^3}$. The sample was mounted on the copper cold finger of a helium dewar, capable of reaching temperatures as low as 10 K. The sample was oriented such that the laser pump pulses propagated along the $\vec{C}$-axis ($\vec{E} \perp \vec{C}$, since $\vec{E}$ is always $\perp$ to the direction of propagation), and the fluorescence was monitored perpendicular to the $\vec{C}$-axis (see Fig. 1).

Sample fluorescence was collected and focused upon the entrance slit of a Spex 1-meter monochromator by a series of lenses. A cutoff filter was inserted at the entrance slit to block the scattered pump laser light. The signal was detected with a 7102 Vis-Near IR photomultiplier tube and processed by a boxcar integrator. The output of the boxcar was recorded on a strip chart recorder.

Two site selective spectroscopy experiments were performed at 10 K using the basic experimental setup shown in Fig. 1: zero order excitation and fluorescence. The zero order excitation experiment varies the excitation wavelength as

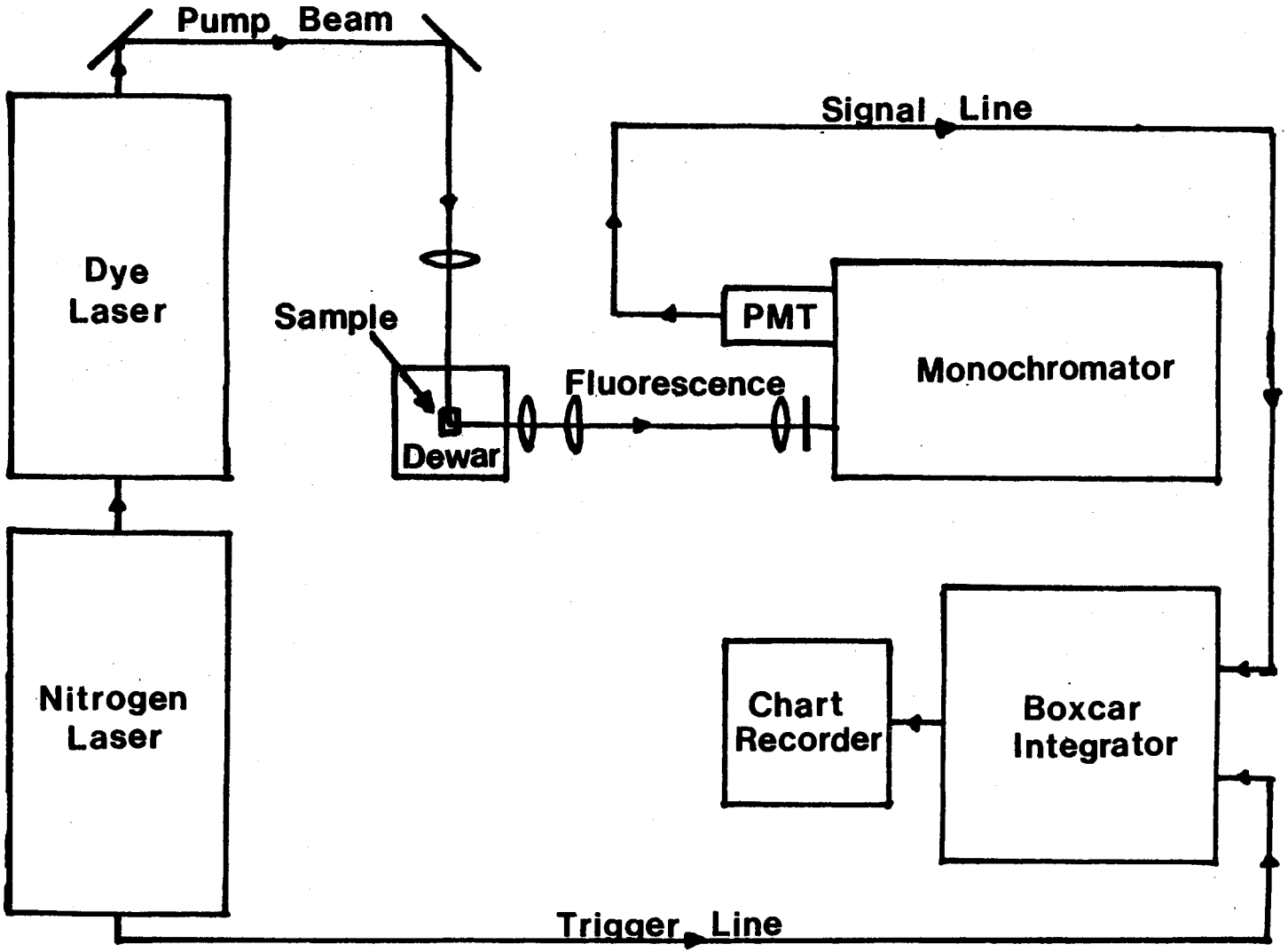

Figure 1. Block Diagram of the Site-Selective Spectroscopy Experiment.

both the delay time (the time elapsed between the instant the pump pulse leaves the laser and when the boxcar begins to integrate the emission signal) and emission wavelength are held constant. It is called "zero order" because the monochromator is set to allow the zero order of the diffraction grating to pass on to the IR detector. In short, the monochromator is effectively removed from the experiment and the entire polychromatic fluorescent emission of the sample is received by the detector. The intensity of the fluorescent emission is plotted versus the excitation wavelength of the dye laser. Because regions of high fluorescent emission are the direct result of strong sample absorption of the excitation wavelength, zero order excitation spectra are an indirect way to determine the spectral positions of the absorption bands of the sample in the tuning region of the laser dye. The advantage of zero order excitation over traditional absorption measurements is that high resolution (on the order of the Full Width at Half Maximum (FWHM) of the dye laser pulse) is obtained without drastic reduction in signal strength.

The fluorescence experiment holds the excitation wavelength constant and varies the monochromator transmission wavelength. The transmitted emission at each wavelength is amplified by the detector and integrated over time by the boxcar. The resulting signal, when plotted versus the monochromator wavelength, gives the spectral dependence of the emission for a known, constant, excitation wavelength. Wavelength resolution is limited by the monochromator slit widths, the monochromator scan speed, and the scroll speed of the strip chart recorder. The high resolution (1 Å) required to distinguish the relative emission wavelengths of the sites necessitates narrow slit widths, slow monochromator scan speeds, and long strip chart recordings. Because narrowing the slits decreases the light gathering capability of the monochromator, the signal strength decreases. This trade-off between intensity and resolution poses problems for site selective fluorescence when the sample emission is weak. The signal to noise ratio for site selective fluorescence measurements was improved by placing a 1 MΩ external load resistor in parallel to the boxcar to reduce the input impedance of the boxcar.

Excitation

Figure 2 is the zero order excitation spectrum of Nd:BMAG for the tuning range of Coumarin-440 dye at 10 K. The spectra has been corrected for filter, grating, and detector response, but not for the dye response. The spectra shows peaks in the 429 to 437 nm range, corresponding to 23,310 to 22,880 cm^{-1}. From the Dieke rare earth energy level diagram [1], the manifolds closest to this energy range are $^2D_{5/2}$, $^2P_{1/2}$, and $^4G_{11/2}$ with approximate free ion energies of 23800, 23200, and 22000 cm^{-1} respectively. The excitation peaks in Fig. 2 are assigned to the $^2P_{1/2}$ manifold because the $^2P_{3/2}$ free ion energy lies within the region where excitation peaks were observed. Since $^2P_{1/2}$ consists of only one Stark component, each peak observed in Fig. 2 is a $^2P_{1/2}$ energy level for the different crystal field sites of Nd^{3+} in BMAG.

The sites associated with the excitation peaks have been labelled in Fig.2. The nomenclature is arbitrary and has no relevance to group theory. Each site has a letter associated with it (i.e. A, B, C, or D) which is useful in catagorizing its gross spectroscopic properties. Low temperature absorption spectra in Nd:$Ba_2ZnGe_2O_7$ (Nd:BZAG) [2], a similar material, reveal only four absorption bands in the $^2P_{1/2}$ spectral region. The absorption peak wavelengths of the four sites in Nd:BZAG agree with the four groupings of excitation peaks observed in Nd:BMAG, so the A, B, C, D-notation established for BZAG was adopted for BMAG as well. The high resolution of zero order excitation showed each letter site to be composed of subsites. Subsites are numbered, with ascending integers indicating descending energy of the $^2P_{1/2}$ manifold.

The intensity of the excitation peaks is directly proportional to the absorption coefficient (see Eq. 56) at the excitation wavelength, the emission strength of the site, and the dye response at the pump wavelength. The exact dye response was not measured, but it is possible to make a few qualitative statements about it: (1) the dye peaks at approximately 433 nm and (2) it tails off at the wavelength limits of the excitation spectra. With this in mind, site A2 is the strongest emitter,

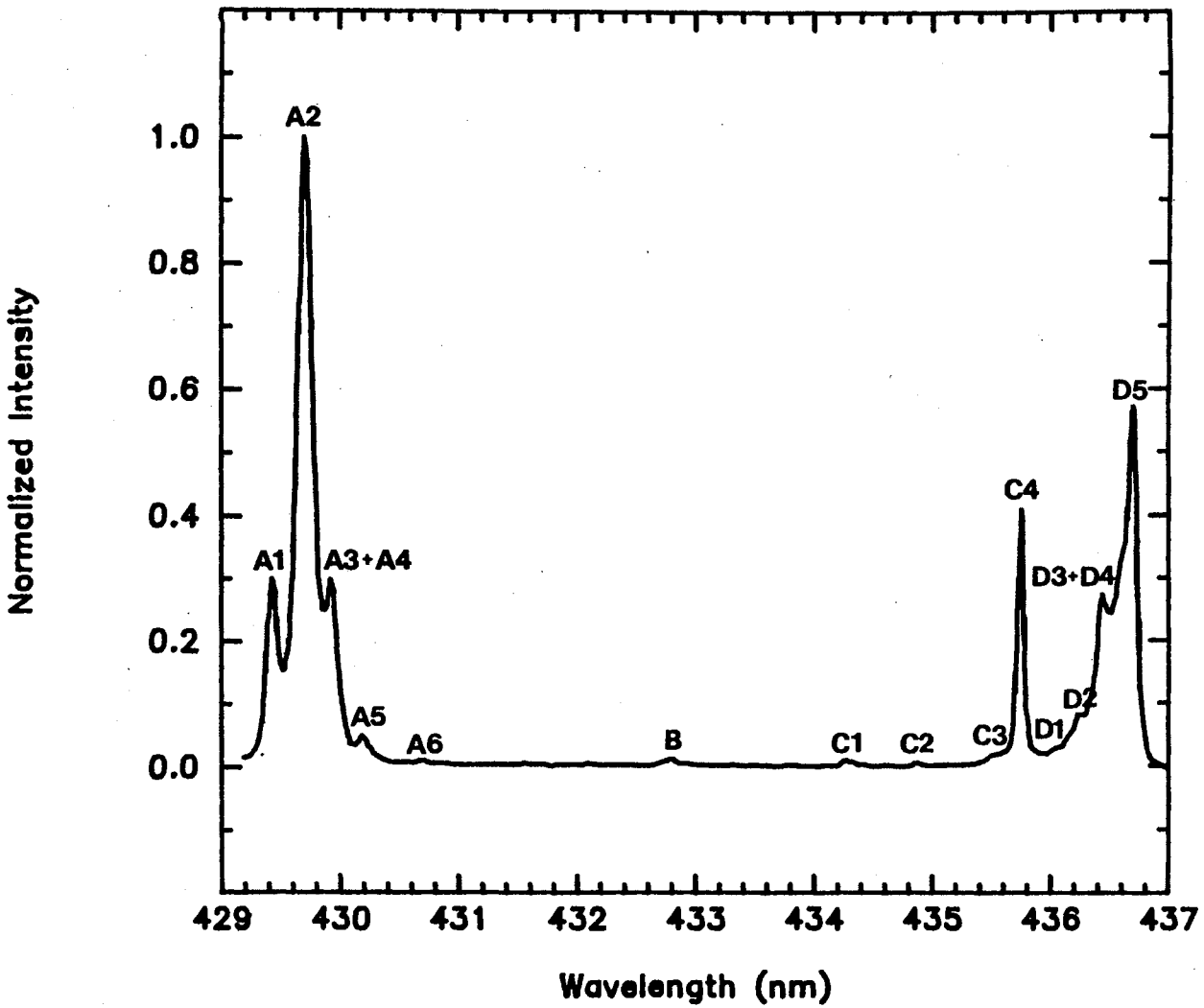

Figure 2. Excitation Spectrum for Coumarin-440 Pumping.

followed closely by sites D5 and C4. Increasing the resolution of the experiment by using an etalon may reveal more sites than the 15 shown in Fig. 2

Although the actual charge compensated substitutional sites associated with the excitation peaks are unknown, comparison of the excitation spectrum of Nd:BMAG with the absorption spectrum of Nd:BZAG shows that the B site is greatly reduced in BMAG. The A, C, and D sites in the two materials have nearly identical spectral shape and relative heights. In Nd:BZAG, the Nd^{3+} ion substitutes for Ba^{2+} easily, Zn^{2+} with difficulty, and never substitutes for Ge^{4+} [2]. The reasoning behind this assertion is that the large Nd^{3+} ion (radius = 0.995 $\AA$) easily can fit into the large Ba^{2+} site (radius = 1.34 $\AA$), has difficulty substituting for Zn^{2+} (radius = 0.74 $\AA$), and is too large to substitute for Ge^{4+} (radius = 0.53 $\AA$) [3]. Under the same argument Nd^{3+} would have greater difficulty substituting for Mg^{2+} (radius = 0.66 $\AA$) in BMAG than Zn^{2+} in BZAG. So under crystal ionic radii considerations, the B site in Nd:BZAG is the Zn^{2+} site, and the A, C, and D sites in BMAG are due to Nd^{3+} substituion for Ba^{2+} or Ge^{4+}.

Figure 3 is the zero order excitation spectrum at 10 K for Rhodomine-590 pumping of the $^2G_{7/2}$ and $^4G_{5/2}$ manifolds. The $^2G_{7/2}$ manifold has four Stark components and $^4G_{5/2}$ has three, so there should be 105 excitation peaks due to the 15 sites in Fig. 3. Only 30 distinct peaks are seen in the excitation spectrum because spectral overlap and stong emission from the A sites obscures the emission from the other weakly emitting sites. This convolution presents a problem for site-selective spectroscopy because single site excitation is impossible, and there is no obvious correspondence between the excitation peaks observed for Rhodimine-590 pumping and the sites revealed by Coumarin-440 pumping.

Fluorescence

With the sites identified by the $^2P_{1/2}$ zero order excitation spectrum, it was possible to pump individual sites with Coumarin-440 dye laser pulses and observe the fluorescence emitted from transitions from $^4F_{3/2}$ to the $^4I_{11/2}$ and $^4I_{9/2}$ manifolds. Absorption band overlap of the different sites is minimal in the

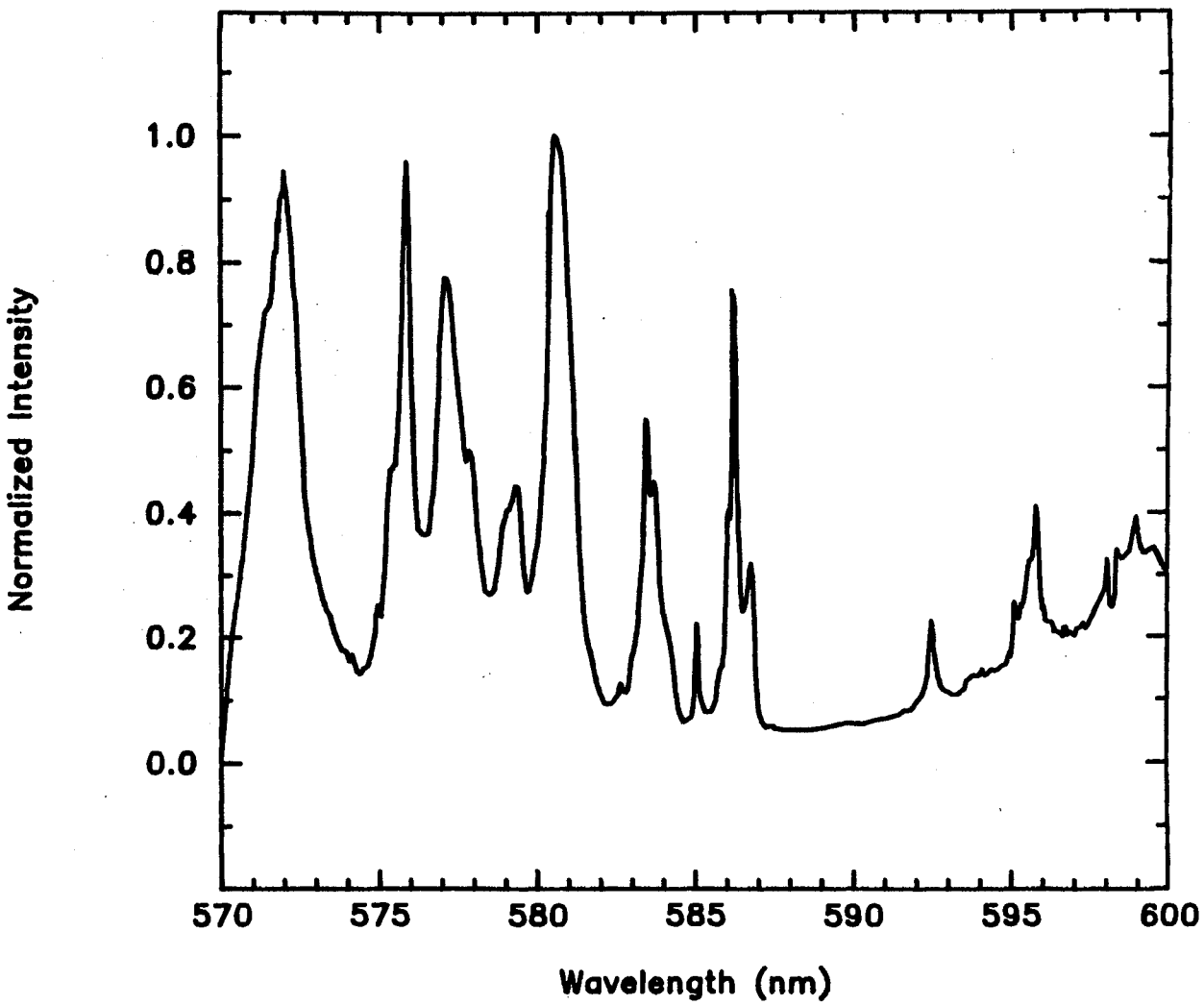

Figure 3. Excitation Spectrum for Rhodimine-590 Pumping.

$^2P_{1/2}$ region, and it is possible to obtain fluorescence spectra free of extraneous lines from other sites. Figure 4 shows three stacked fluorescence spectra at 10 K indicative of sites A2, C4, and D5 for $^2P_{1/2}$ pumping. Energy transfer between sites is inhibited at 10 K (discussed later), so when electrons of a particular site are excited to the $^2P_{1/2}$ level, they radiatively relax and emit fluorescence characteristic of the site pumped. The fluorescence peaks have intensity proportional to the transition dipole moment and a wavelength proportional to the separation between the electronic energy levels of the site.

The low wavelength, high intensity peak within each spectrum in Fig. 4 is the transition between the lowest lying Stark levels of the $^4F_{3/2}$ and $^4I_{11/2}$ manifolds, and is the one that is expected to lase. These highly intense "laser transitions" appear at distinctly different wavelengths between sites with different letter labels (i.e. A vs. D). A rough rule of thumb is 1050, 1060, 1070, and 1080 nm for sites A, B, C, and D respectively. As discussed earlier, these letter sites are believed to be different substitutional sites for Nd^{3+} in the BMAG host (i.e. Nd^{3+} substituted for Ba). The lasing wavelengths differ among sites by amounts similar to that for Nd^{3+} between hosts. Such large perturbations in the energy levels are due to distinctly different local crystal fields, and the simplest explanation for large variation of the local crystal field between sites is substitution.

The lasing wavelengths of the numbered sites of the same letter (i.e. A1, A2, A3, ...) have wavelengths which vary by 5 to 10 angstroms. Because the spectroscopic differences are minimal between these sites, they are called "subsites". The subsites are believed to be distinguished by perturbations in the substitional site crystal field due to inhomogeneities about the substitutional site (lattice defects, impurities, nearest neighbor Nd^{3+} ions, etc.).

Selectively pumping the different excitation peaks in the $^2P_{1/2}$ spectral region lead to the identification of the lowest lying Stark levels of the $^4F_{3/2}$, $^4I_{11/2}$, and $^4I_{9/2}$ manifolds for the fifteen sites of Nd:BMAG. The excitation spectrum of the $^2G_{7/2} + {}^4G_{5/2}$ manifolds promised severe problems for site selection. Only 30 of the 105 excitation peaks were distinct in the zero order excitation spectrum,

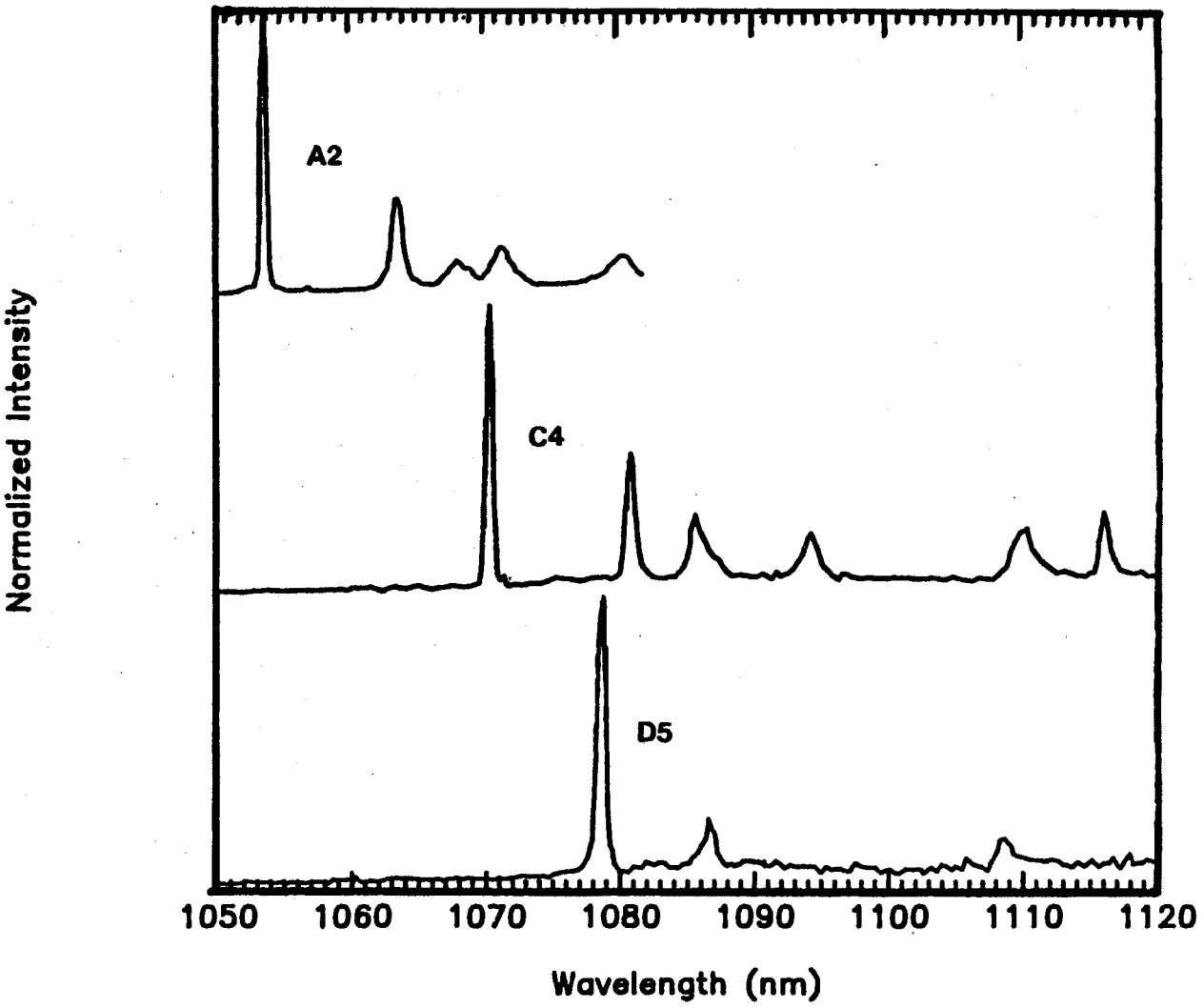

Figure 4. Fluorescence from $^4F_{3/2}$ to $^4I_{11/2}$ Transitions for Different Sites at 10 K.

so absorption band overlap and multi-site emission were expected to make interpretation of the fluorescence spectra difficult. The problem was resolved using tuning/detuning techniques.

Tuning and detuning at 10 K were key experimental techniques for determining the sites in the $^2G_{7/2} + {}^4G_{5/2}$ multiplets. Figure 5 shows a representative spectra where a "tuned" and "detuned" spectra are overlaid. Comparison of the relative line strengths between the tuned and detuned spectra determines the fluorescence peaks associated with each excitation. The dashed "detuned" spectra is the fluorescence recorded when the sample was pumped two angstroms below the 585.8 nm excitation peak. The detuned spectra has emission at 1052 and 1053.5 nm corresponding to the lasing transitions for sites A1 and A2. The solid spectrum is the fluorescence observed when the excitation wavelength is "tuned" to the excitation peak. The absence of the 1052 nm emission in the tuned spectrum infers that the excitation peak at 585.8 nm corresponds to the site that emits at 1053.5 nm, site A2. It is interesting to note what a dramatic difference a slight change in excitation wavelength has upon site selection for the broad excitation peaks in Fig. 3.

The results of the spectroscopic energy level identification for the sites of Nd:BMAG at 10 K are presented in Fig. 6 and Table I. The energy of the levels generally decrease from sites A to D. Although the splittings of individual multiplets are precise to within 5 cm^{-1}, the absolute energy of the multiplet has an accuracy 30 cm^{-1}. The poor accuracy is due to daily variations in the spectrometer and backlash in the dials, and the high precision is due to high resolution within a scan.

To briefly summarize, zero order excitation of the $^2P_{1/2}$ spectral region in Nd:BMAG reveals fifteen distinct nonequivalent crystal field sites for Nd^{3+} in the BMAG host. The energy levels are proposed to be strongly perturbed by the substitution site (letter label), and weakly perturbed by inhomogeneities about the substitution site (number label). Comparison of atomic radii and absorption

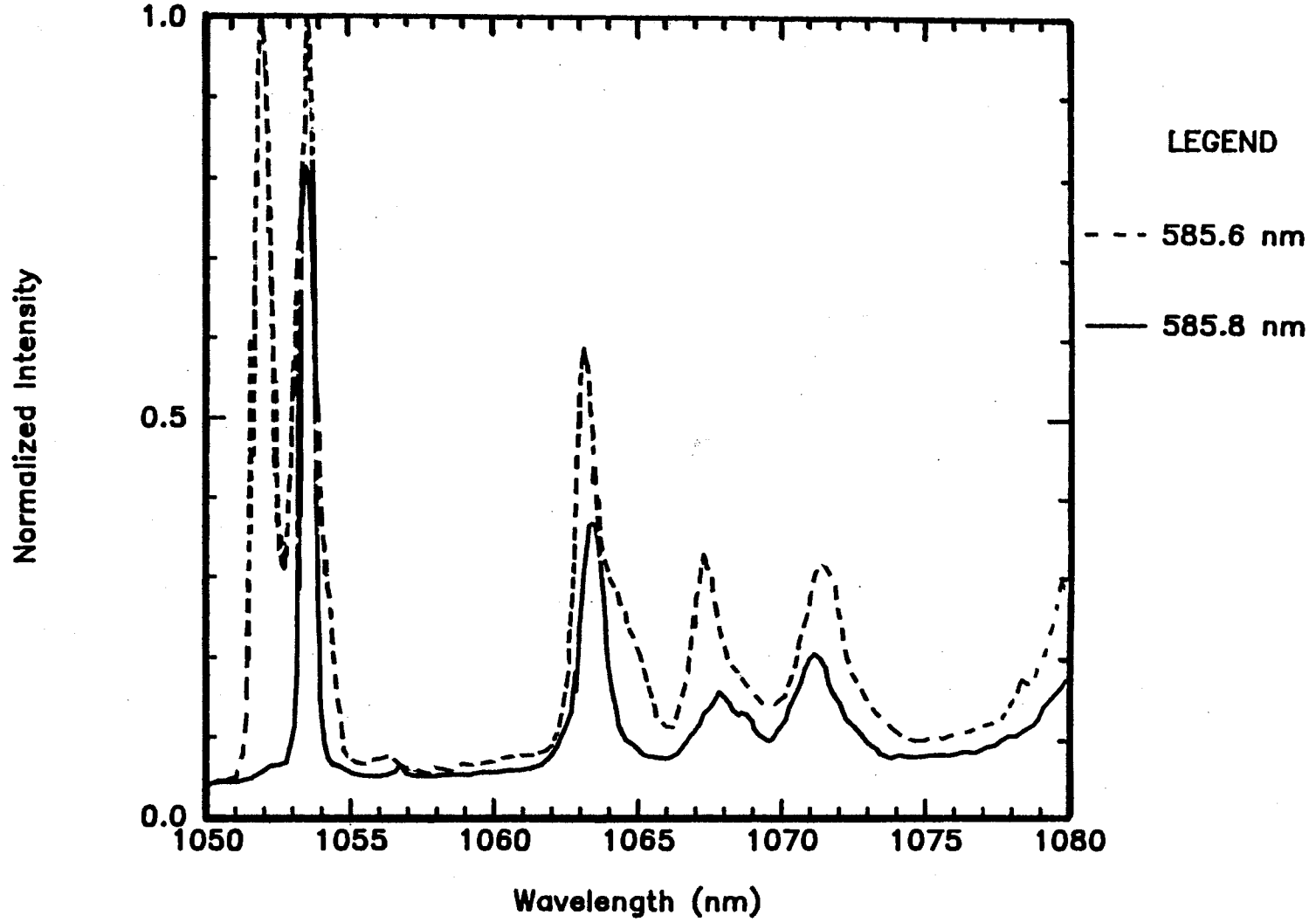

Figure 5. Tuned and Detuned Fluorescence for Rhodimine-590 Pumping.

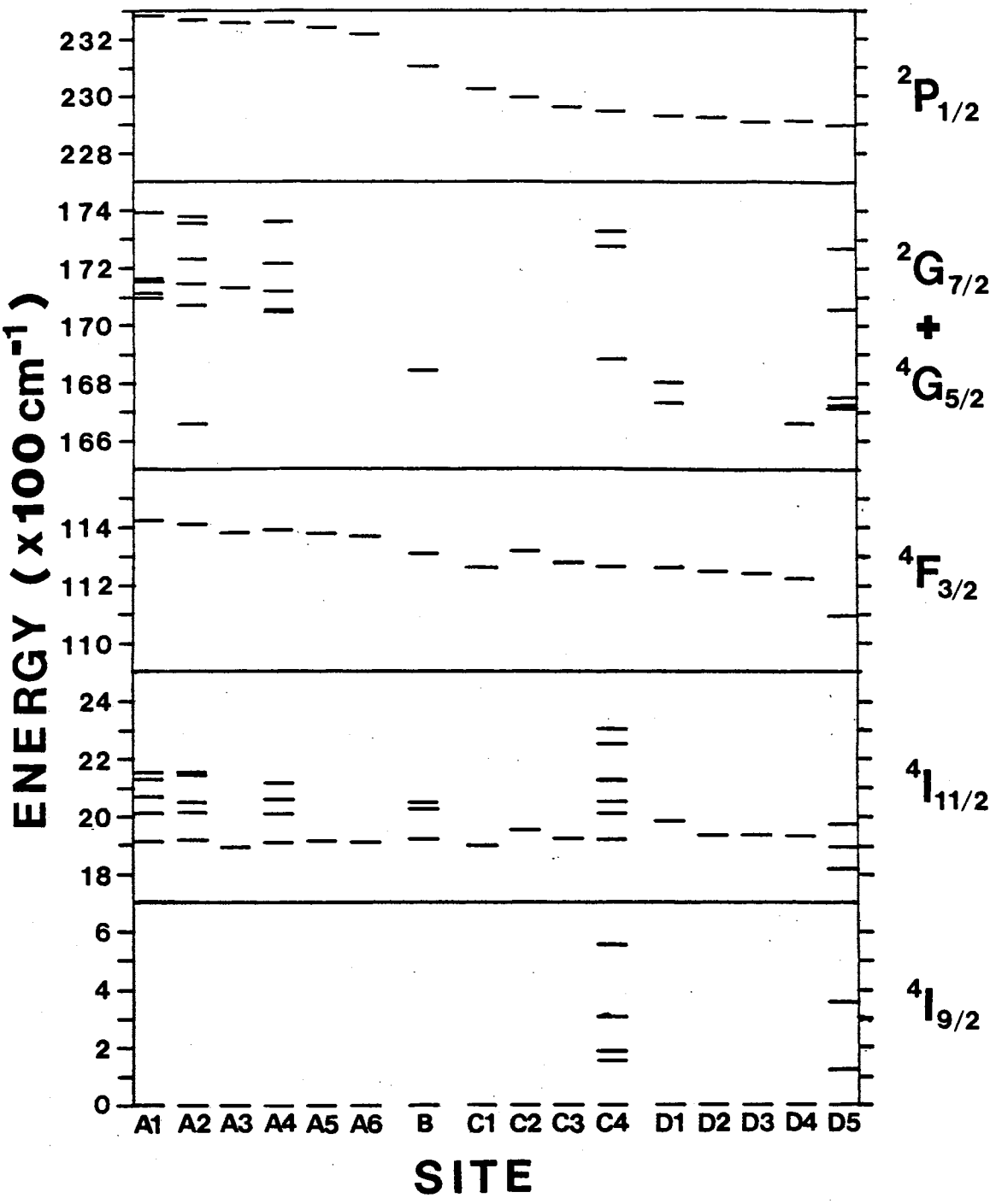

Figure 6. Energy Level Diagram for the Different Crystal Field Sites in Nd:BMAG at 10 K.

TABLE I

EXPERIMENTAL ENERGY LEVELS OF THE CRYSTAL FIELD SITES OF Nd:BMAG AT 10K.

Site Label	Manifold $^4I_{9/2}$	$^4I_{11/2}$	$^4F_{3/2}$	$^2G_{7/2} + {}^4G_{5/2}$	$^2P_{1/2}$
A1	0	1915	11423	17076	23285
		2011		17097	
		2068		17161	
		2129		17355	
		2149		17394	
A2	0	1921	11414	17071	23271
		2015		17138	
		2048		17229	
		2142		17346	
		2156		17379	
A3	0	1896	11383	17123	23261
				17132	
A4	0	1910	11393	17047	23261
		2004		17218	
		2060		17364	
		2117			
A5	0	1915	11380		23243
A6	0	1910	11370		23220
B	0	1921	11312		23107
		2024			
		2048			

TABLE I (Continued)

Site Label	Manifold $^4I_{9/2}$	$^4I_{11/2}$	$^4F_{3/2}$	$^2G_{7/2} + {}^4G_{5/2}$	$^2P_{1/2}$
C1	0	1901	11259		23027
C2	0	1958	11321		22996
C3	0	1925	11280		22961
C4	0	1919	11263	16697	22948
	156	2012		16883	
	188	2052		17091	
	304	2123		17328	
	555	2253			
		2303			
D1	0	1984	11260		22933
D2	0	1935	11249		22924
D3	0	1935	11240		22911
D4	0	1932	11226	16661	22911
				16798	
				16846	
D5	0	1823	11095	16661	22897
	130	1898		16716	
	360	2074		16725	
				16750	
				16793	
				16801	
				17304	

of Nd:BZAG with zero order excitation of Nd:BMAG lead to the tentative identification of Ba^{2+} and Ge^{4+} as probable substitutional sites in the host associated with sites A, C, and D for Nd:BMAG. Fluorescence at 10 K shows that the lasing transition wavelength ranges from 1050 to 1080 nm depending upon the site.

CHAPTER II

ENERGY TRANSFER

Experiment

The energy transfer experiment was designed to increase the sample temperature in 30 degree intervals from 10 K, and search for time dependent energy transfer at each temperature. The $^2P_{1/2}$ level was selected as the pump level to minimize multi-site emission due to absorption band overlap at the excitation wavelength. The fluorescence from the $^4F_{3/2}$ to $^4I_{11/2}$ transitions was monitored because of the high intensity and large wavelength separation of the lasing transitions for the different sites.

The experimental arrangement for the energy transfer studies is the same as that shown in Fig. 1. A 60 watt heater coil mounted upon the cold finger of the dewar was used to elevate the sample temperature from 10 K. A thermal diode was used to monitor the temperature at the sample, and a Lake Shore Cryotonics heater control unit was used to set and regulate the sample temperature. Coumarin-440 dye was used in the Molectron nitrogen pumped dye laser to optically pump the $^2P_{1/2}$ level for each site. The emission scan range was limited from 1045 to 1080 nm, the range in which the lasing transitions appear for the fifteen sites. The boxcar integrator was set to three different delay times for each temperature: 10 μs, 200 μs, and 1 ms. The spectral resolution (slit dispersion limited) was 0.5 nm. The external load resistor was 200 kΩ, well under the RC time distortion limit ($\tau_{circuit} \approx 0.2$ μs versus $\tau_{spont} \approx 350$ μs).

Temperature and Time Dependent Fluorescence

Energy transfer between nonequivalent crystal field sites in Nd:BMAG is predicted from the appearance of the room temperature fluorescence spectrum

for ${}^4F_{3/2} \rightarrow {}^4I_{11/2}$ emisssion. Figure 7 is the room temperature fluorescence of Nd:BMAG for 589.0 nm excitation. The fluorescence bands are broad and indicative of A site emission. Pumping any site at room temperature results in the emission shown in Fig. 7, inferring that energy is being completely transferred to site A at room temperature.

The choice of the sites to study for energy transfer was made with several considerations in mind. Since the emission lines broaden with increasing temperature, resolution of energy transfer between numbered sites of the same substitional site (i.e. A3 to A2) would be difficult, if not impossible. No energy transfer was observed in preliminary experiments from site A to the other letter sites so A pumping was ruled out. Because both temporal and spectral resolution were required, high emission intensity was necessary. The zero order excitation spectra for Coumarin-440 pumping shows that sites D5 and C4 both are intense emitters, with negligible absorption band overlap with other sites in the ${}^2P_{1/2}$ region. Sites D5 and C4 were consequently selected for the energy transfer study.

Figure 8 is a composite of all the temperature dependent fluorescence spectra for D5 site pumping at a time delay of 200 μs after the pulse. The peak at 1078 nm is the laser transition for the site D5, and the emission at 1053.5 to 1054.5 nm is the lasing transition for site A2, thermally shifted to a higher wavelength. Both emission peaks broaden and shift with increasing temperature. The energy of the optically pumped sensitizer, site D5, is seen to transfer to the activator, site A2.

No time dependence of the relative line strengths was noted at any temperature in the energy transfer study. Figure 9 expresses the null result for the arbitrary temperature of 160 K and temporal gate width of 0.5μs. Three times are represented: 10 μs, 200 μs, and 1 ms. A delay of 10 μs is on the rise time portion of the lasing transition fluorescence curve, and is the shortest time delay set for which one could maintain a feasible signal to noise ratio in the spectra. Similarily, 1 ms is the latest point in time for acceptable signal to noise ratio. The delay of 200 μs corresponds roughly to the peak fluorescent emission in time. The three traces in Fig. 9 agree within experimental error. Differences in shape of the lines

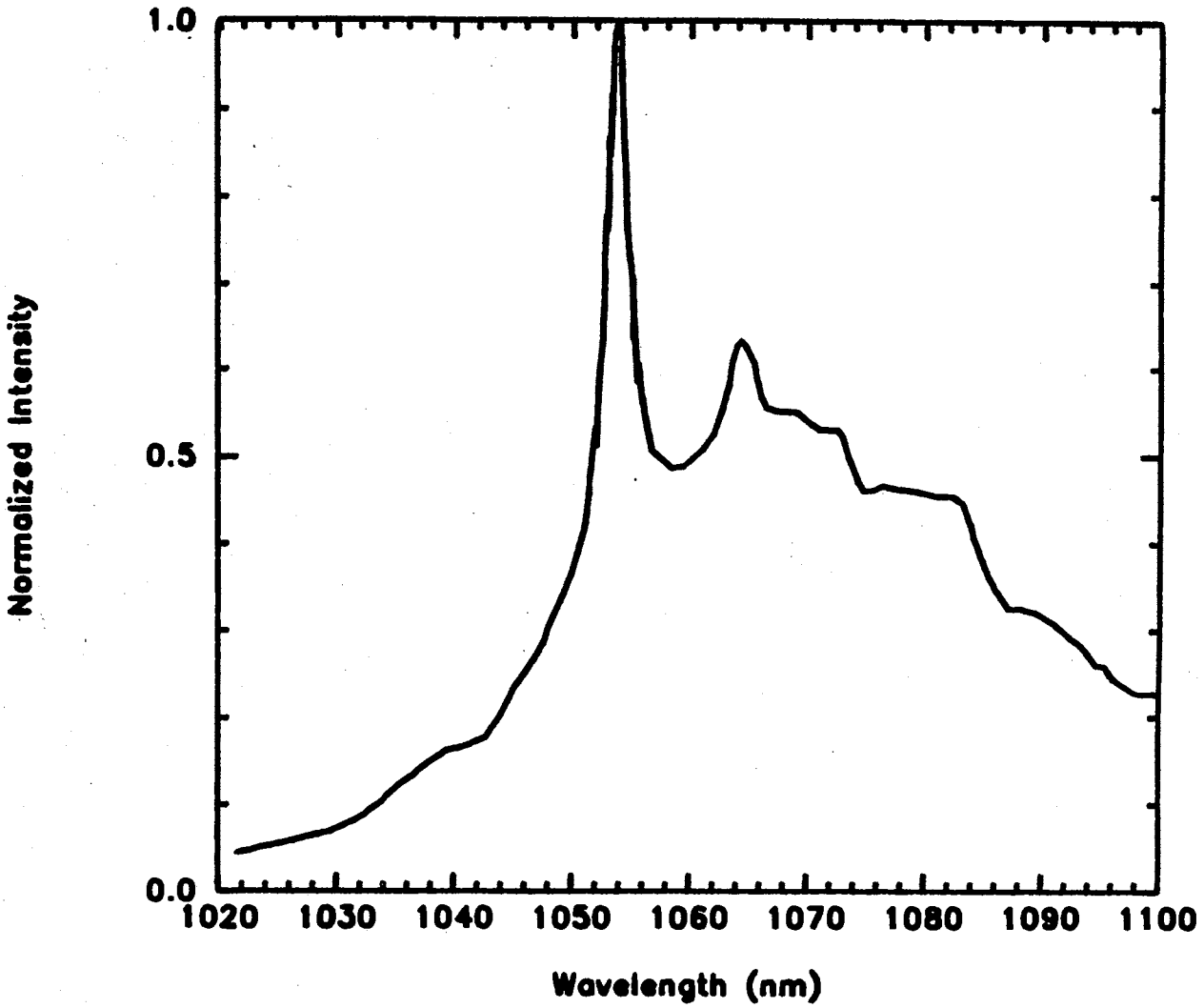

Figure 7. Fluorescence at Room Temperature of Nd:BMAG for Transitions Between the $^4F_{3/2}$ and $^4I_{9/2}$ Manifolds.

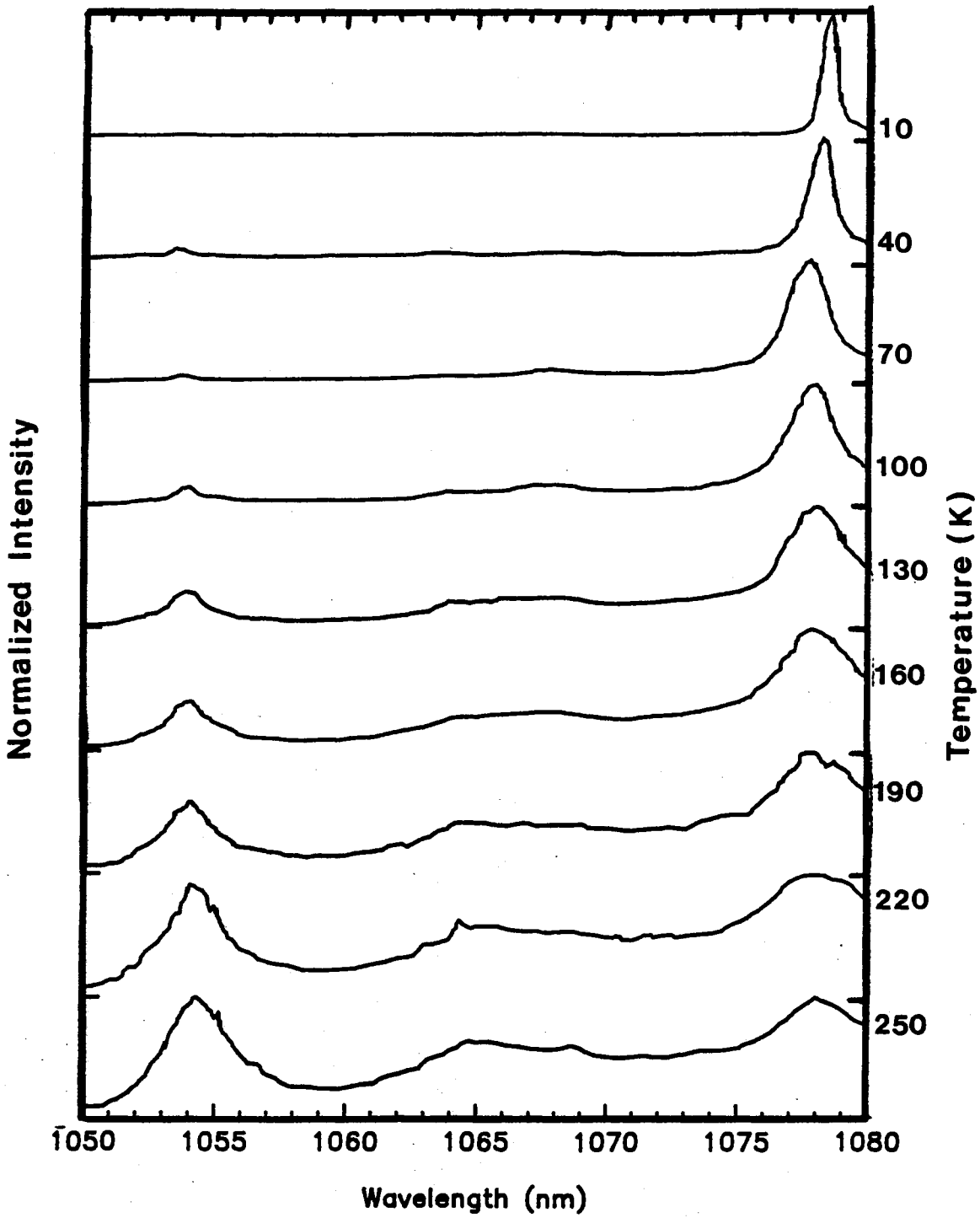

Figure 8. Temperature Dependent Energy Transfer for Site D5 Pumping in Nd:BMAG.

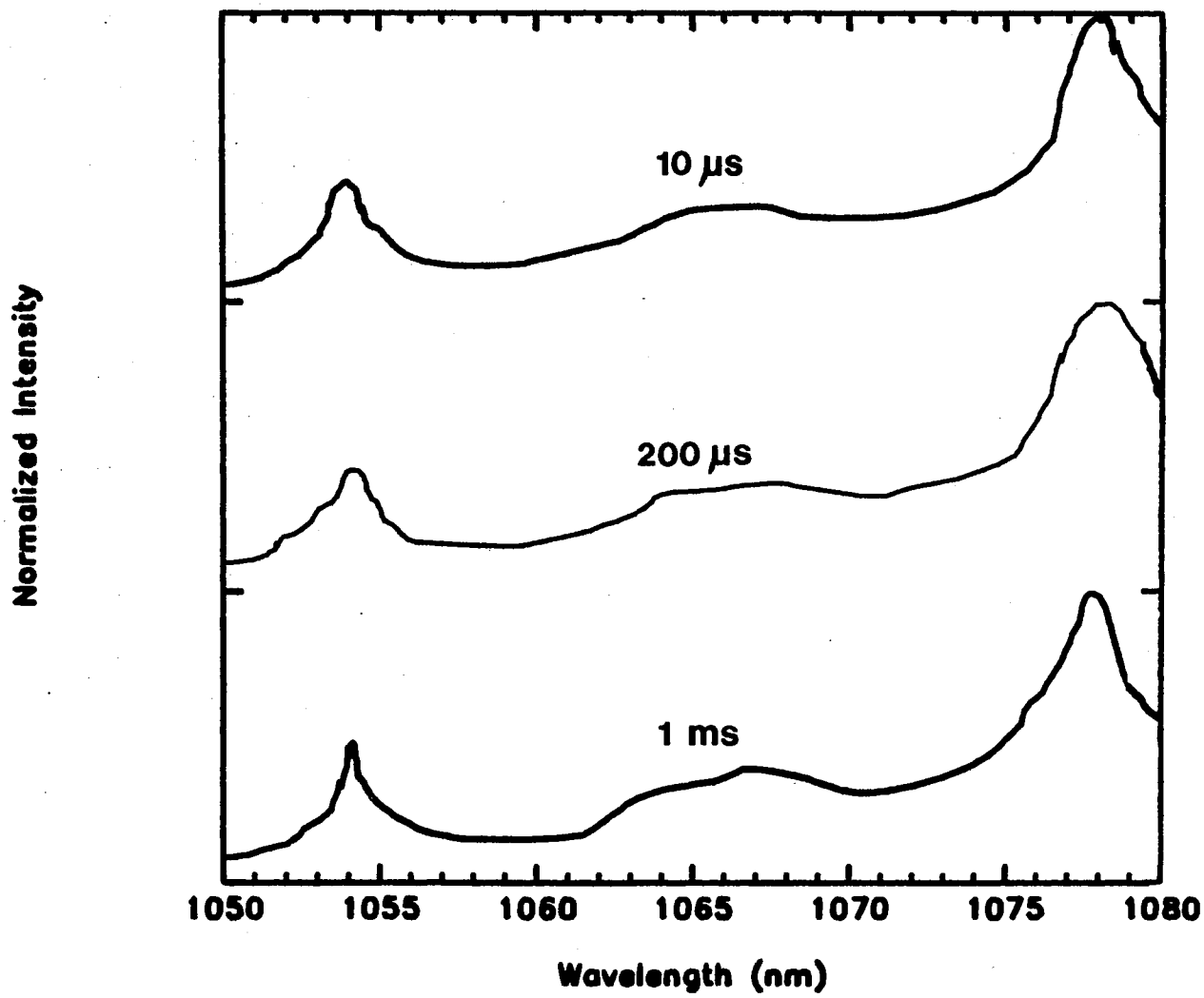

Figure 9. Time Dependent Fluorescence for Site D5 Pumping at 160 K.

can be attributed to manual digitization of analog signals with large signal to noise ratios.

The lack of any time dependence seen at 160 K in Fig. 9 is representative for all temperatures studied. The integrated intensity ratios of the lasing transitions for sites D5 and A2 remained constant within experimental error over the entire time domain of the fluorescent emission accessible by the experiment (10 μs to 1ms). This leads to the conclusion that either the energy transfer occurs during the nonradiative relaxation from the $^2P_{1/2}$ pump level to the $^4F_{3/2}$ storage level, or resonant transfer is thermally activated between the Stark components of the $^4F_{3/2}$ manifolds of the two sites. Either conclusion addresses the fact that the energy transfer is completed prior to $^4F_{3/2}$ emission.

Figure 10 is the temperature dependent energy transfer from the optically pumped sensitizer, C4, to the activator, A2, at 200 μs after the pulse. Like the D5 energy transfer scenario, energy transfer from site C4 (emission wavelength = 1070 nm) is thermally activated and time independent. The activator, A2, emits at 1053.5 nm at low temperatures and is thermally shifted to 1054.5 nm at high temperatures. The transfer from site C4 is thermally activated at a lower temperature than the D5 transfer.

Theory of Energy Transfer

The model used to explain the temperature dependent energy transfer is shown in Fig. 11. The sensitizer, S, is the site that is optically pumped (site C4 or D5). The activator, A, is the site to which energy is transferred (site A2). The energy levels of the sensitizer and activator are displayed side by side. The labels S1, S2, S3, A1, and A2 in Fig. 11 represent Nd^{3+} ion concentrations in the energy levels of the sensitizer and activator, and will also be used to refer to particular manifolds and levels of the sites. The $^4I_{9/2}$ manifolds for the sensititizer and activator have ion concentrations S1 and A1. The lowest lying Stark energy level of $^4F_{3/2}$ for the sensitizer is the "metastable state", and has a concentration S2. S3 is the ion concentration of the high energy Stark component of $^4F_{3/2}$, or

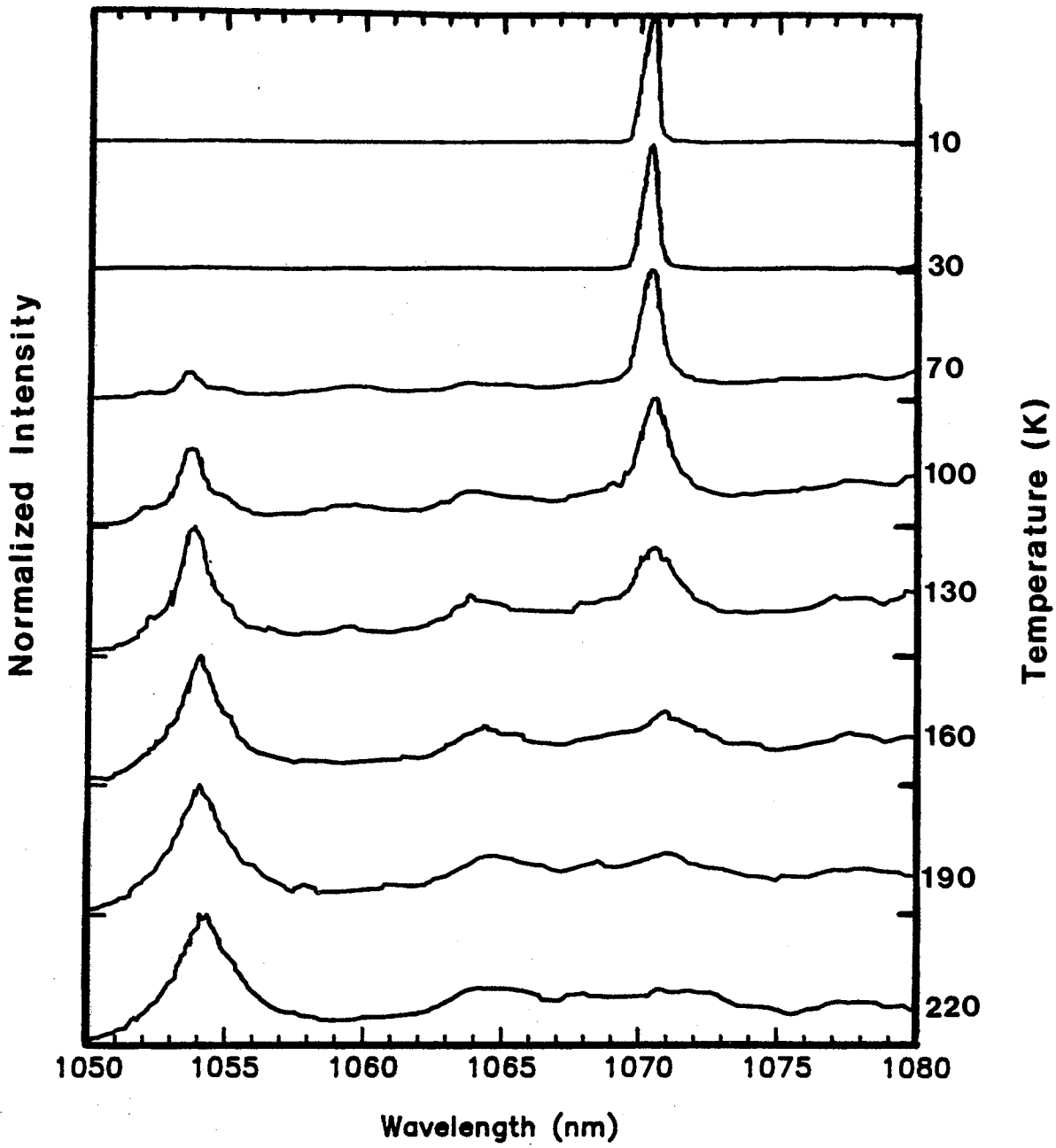

Figure 10. Temperature Dependent Energy Transfer for C4 Site Pumping in Nd:BMAG.

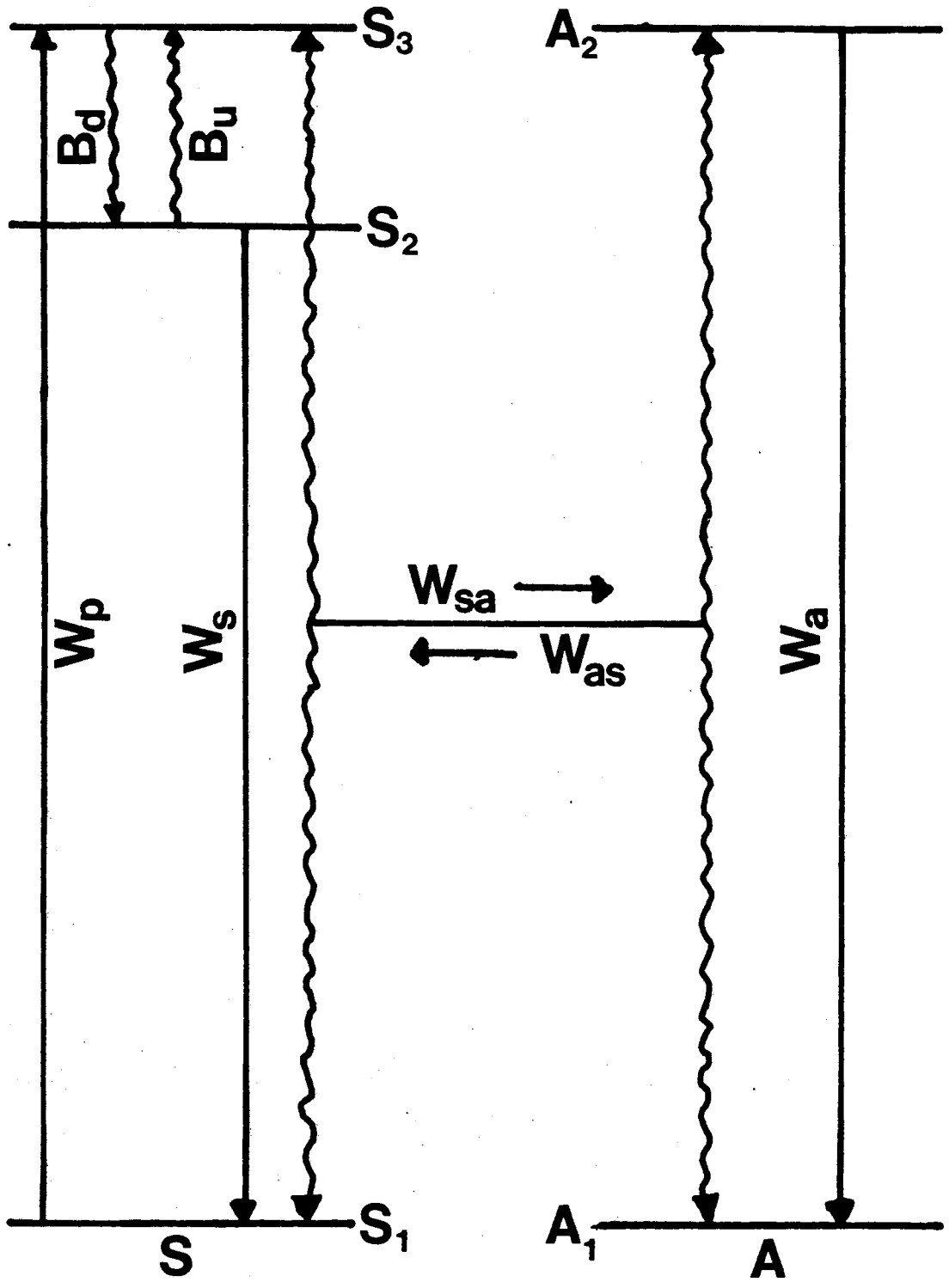

Figure 11. Model Used to Explain the Temperature Dependent Energy Transfer Observed in Nd:BMAG.

the "hot band" of the sensitizer. S2, is referred to as the "hot band" because its population with respect to the metastable state is governed by a Boltzmann constant. The metastable state of the activator has a concentration, A2. As temperature increases, the hot band of the sensitizer broadens and overlaps the metastable state of the activator.

The pump rate, W_p, involves absorption from $^4I_{9/2}$ to $^2P_{1/2}$, and fast non-radiative relaxation to $^4F_{3/2}$. In Fig. 11, S3 is effectively populated by the pump rate. The thermal population of the hot band is described by "up" and "down" Boltzmann rates (e.g. B_u and B_d are the "up" and "down" rates for the sensitizer). The Stark components of the $^4F_{3/2}$ manifold of the sensitizer are separated by an energy gap, ΔE_s. Ions decay from the metastable state to $^4I_{9/2}$ with rates W_s and W_a for the sensitizer and activator.

Energy transfer between ions is described by a forward rate, W_{sa} (from sensitizer to activator), and a back transfer rate, W_{as} (from activator to sensitizer). Forward energy transfer involves the demotion of a sensitizer ion from S3 to S1 with the simultaneous promotion of an activator ion from A1 to A2. The back transfer process involves demotion from A2 to A1 and promotion from S1 to S3. It is important to realize that no electrons are transferred between the sites even though the energy transfer process may be thought of as an excited electron (exciton) moving from ion to ion in the crystal lattice. Because the process is only resonant between S3 and A2, thermal population of S3 is required (and no transfer is observed at low temperatures).

The goal of using the rate equation approach is to determine the functional dependence of the ratio of the activator and sensitizer intensities. The intensity ratio is proportional to the ratio of the number of ions in the metastable states of the sensitizer and activator. The emission intensity, I, is related to the excited state ion concentration, n by

$$I = Wn \tag{1}$$

where W is the rate of spontaneous emission. So the activator to sensitizer intensity ratio is

$$\frac{I_a}{I_s} \approx \frac{W_a A_3}{W_s S_2} \tag{2}$$

where I_a and I_s are the integrated intensities of the lasing transitions for the activator and sensitizer. Equation 2 is approximately equal because I in Eq. 1 is the intensity emitted over all solid angle. The intensities in the temperature dependent energy transfer experiment were measured for a limited solid angle in one crystal orientation and are not equal to I in Eq. 1.

The rate equations for the energy transfer model are:

$$\dot{S}_1 = -W_p S_1 + W_s S_2 + W_{sa} S_3 - W_{as} A_2 \tag{3}$$

$$\dot{S}_2 = -W_s S_2 - B_u S_2 + B_d S_3 \tag{4}$$

$$\dot{S}_3 = +W_p S_1 - W_{sa} S_3 + W_{as} A_2 + B_u S_2 - B_d S_3 \tag{5}$$

$$\dot{A}_1 = +W_a A_2 - W_{sa} S_3 + W_{as} A_2 \tag{6}$$

$$\dot{A}_2 = -W_a A_2 + W_{sa} S_3 - W_{as} A_2 \tag{7}$$

The five coupled rate equations may be simplified and solved by appealing to the qualitative results of the temperature dependent energy transfer experiment. The first simplification is realizing that the 10 μs pump pulse may be treated as a delta function, with a finite number of excited ions populating S3 after the pulse duration. So the pump rate may be set equal to zero in the rate equations after S3 is populated. This is a reasonable simplification because the energy transfer experiment is insensitive to the transient effects associated with the pump pulse.

The next simplifications involve the relative magnitudes of the rates in the rate equations. Because experiment shows that the relative intensities of the lasing transitions are time independent for delays as fast as 10 μs, the energy transfer rates must be greater than $\frac{1}{10\mu s} = 10^5$ Hz. The rate of decay to the ground state

is the inverse of the fluorescence lifetime $\frac{1}{350\mu s} = 2.86 \times 10^3$ Hz. So the energy transfer rates are much greater than the fluorescent decay rates,

$$W_{sa}, W_{as} \gg W_s, W_a. \tag{8}$$

Similarily, the Boltzmann rates in the model must be faster than the transfer rates. Boltzmann rates depend upon phonon emission and absorption. The small wavenumber separation of S2 and S3 (≤ 300 cm^{-1}) may be bridged by single phonon absorption or emission. The nonradiative rate for a Germanate crystal host is greater than 10^9 Hz for a single phonon process [4]. Energy transfer rates between Nd^{3+} ions in garnet hosts [5] were found to be much slower ($\approx 10^3$ Hz). Although the energy transfer experiment does not directly determine the energy transfer rate, the approximation

$$B_u, B_d \gg W_{sa}, W_{as} \tag{9}$$

is reasonable and in agreement with results from other materials. If the Boltzmann rates were slower than the transfer rates, the model in Fig. 11 would predict that transfer between ions would dominate and depopulate S3 regardless of temperature, and the relative line strengths of the sensitizer and activator would be temperature independent.

The final simplification involves applying the steady state solution to the rate equations. The basic idea of a steady state solution is that the ion concentrations in all states are static. Steady state is reached in this system at a time between the initial population of S3 via the pump pulse, and the onset of fluorescent decay from the metastable states ($\approx 10\mu$s). The steady state approximation is plausible in this time regime because the finite number of excited ions are driven to fixed distributions among the $^4F_{3/2}$ levels of the sensitizer and activator (rapid Boltzmann and energy transfer rates quickly establish equilibrium between S2, S3, and A2). The fluorescent decay in this time regime is inconsequential, so the excited ion population remains constant. If the excited states did not reach equilibrium, the energy transfer observed in the fluorescence would be time dependent.

Assuming the delta function pump pulse and retaining the dominant terms as defined by Eqs. 8 and 9, the steady state rate equations become

$$\dot{S}_1 = 0 = +W_{sa}S_3 - W_{as}A_2 \tag{10}$$

$$\dot{S}_2 = 0 = -B_u S_2 + B_d S_3 \tag{11}$$

$$\dot{S}_3 = 0 = +B_u S_2 - B_d S_3 \tag{12}$$

$$\dot{A}_1 = 0 = -W_{sa}S_3 + W_{as}A_2 \tag{13}$$

$$\dot{A}_2 = 0 = +W_{sa}S_3 - W_{as}A_2 \tag{14}$$

Equations 11 and 12 can be rewritten as

$$\frac{S_3}{S_2} = \frac{B_u}{B_d}. \tag{15}$$

The ratio of the Boltzmann rates may be determined by a Boltzmann exponential [6], so Eq. 15 becomes

$$\frac{S_3}{S_2} = e^{-\frac{\Delta E_s}{k_B T}} \tag{16}$$

where k_B is Boltzmann's constant and T is the temperature. Equations 10, 13, and 14 may be written as

$$\frac{A_2}{S_3} = \frac{W_{sa}}{W_{as}}. \tag{17}$$

Combining Eqs. 16 and 17, the ratio of ion concentrations in the metastable states of the activator and sensitizer may be written as

$$\frac{A_2}{S_2} = \frac{A_2}{S_3}\frac{S_3}{S_2} = \frac{W_{sa}}{W_{as}} e^{-\frac{\Delta E_s}{k_B T}}. \tag{18}$$

The rates of fluorescent emission are inversely proportional to the fluorescent lifetime,

$$W_s = \frac{1}{\tau_s} \tag{19}$$

$$W_a = \frac{1}{\tau_a} \tag{20}$$

where τ_s and τ_a are the lifetimes of the sensitizer and activator. The integrated intensity ratio may be written by combining Eqs. 2, 18, 19, and 20 as

$$\frac{I_a}{I_s} \approx \frac{\tau_s}{\tau_a}\frac{W_{sa}}{W_{as}} e^{-\frac{\Delta E_s}{k_B T}}. \tag{21}$$

Equation 21 states that the activator to sensitizer integrated intensity ratio is proportional to an exponential activation energy involving the energy gap among the $^4F_{3/2}$ components of the sensitizer. The constant of proportionality depends upon the ratio of forward to back transfer rates, and also depends upon the ratio of sensitizer to activator lifetimes. Although Eq. 21 was derived for the time regime before fluorescence, the equation is valid during fluorescent emisson because the fluorescence lifetimes for the sites at high temperatures (on the order of the activation temperature for energy transfer) are equal. This is easily demonstrated by assuming an exponential decay to describe the time dependence,

$$I(t) = I(t=0)e^{\frac{-t}{\tau}}. \tag{22}$$

The time-dependent intensity ratio becomes

$$\frac{I_a(t)}{I_s(t)} = \frac{I_a(t=0)}{I_s(t=0)} e^{-t(\frac{1}{\tau_a}-\frac{1}{\tau_s})}. \tag{23}$$

With $\tau_a = \tau_s$, the intensity ratio becomes time independent

$$\frac{I_a(t)}{I_s(t)} = \frac{I_a(t=0)}{I_s(t=0)} \tag{24}$$

and the intensity ratios reduce to the form of Eq. 21. Because the data suggests that the lifetimes of the sensitizer and activator are equal, Eq. 21 may be simplified as

$$\frac{I_a}{I_s} \approx \frac{W_{sa}}{W_{as}} e^{-\frac{\Delta E_s}{k_B T}}. \tag{25}$$

Figure 12 plots the natural log of the activator to sensitizer intensity ratio versus inverse temperature for C4 and D5 site pumping. The integrated intensities were determined by Gaussian fits of the lasing transition emission verses temperature. Good Gaussian fits were only obtained over a limited temperature region. At low temperatures, the activator emission was too small to accutately integrate.

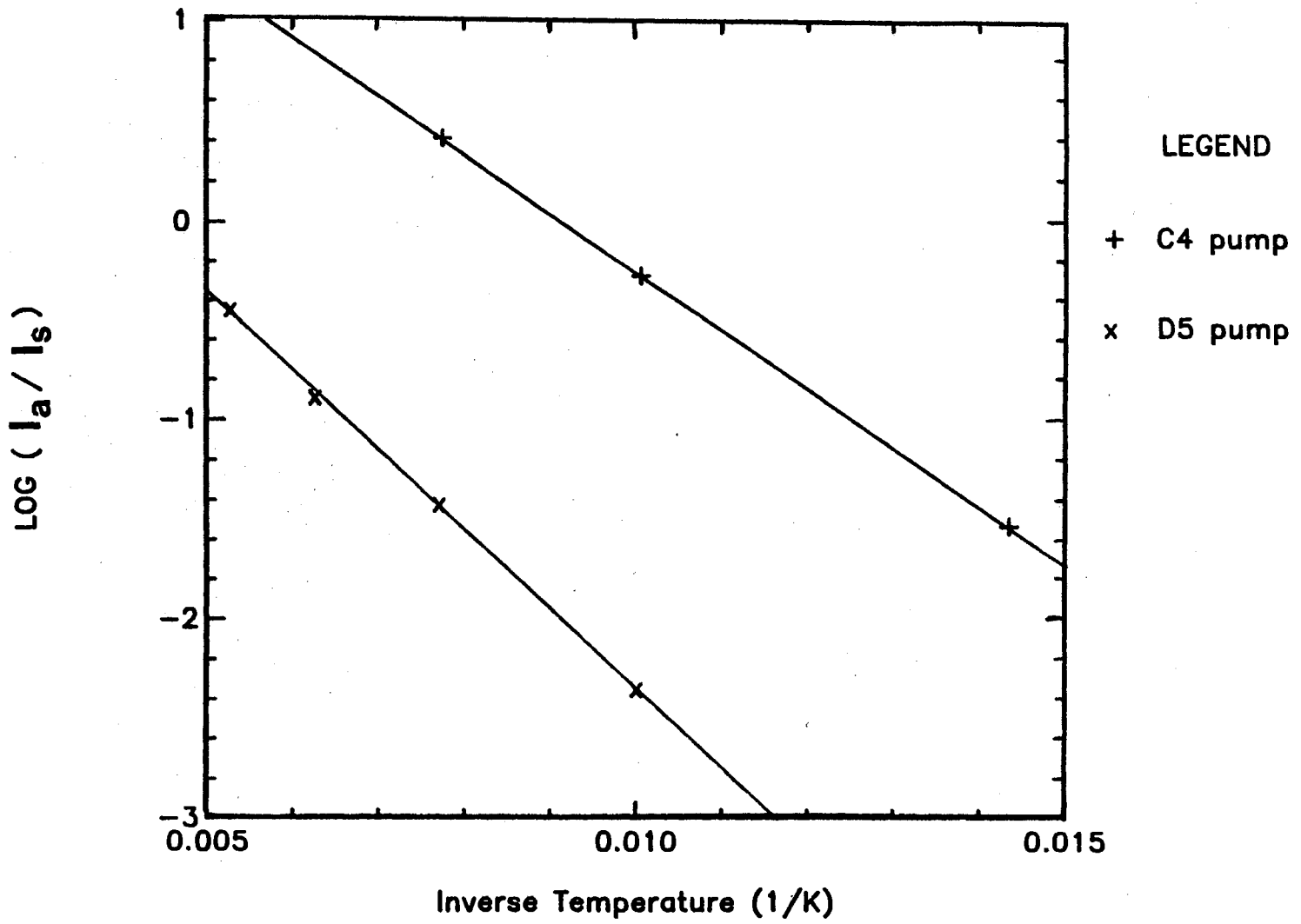

Figure 12. Activation Energy Plot for the Sensitizers C4 and D5 and the Sole Activator, A2.

TABLE II

EXPERIMENTAL ENERGY TRANSFER PARAMETERS FOR THE SENSITIZERS C4 AND D5

Sensitizer	ΔE_s	$\frac{W_{sa}}{W_{as}}$	ΔE_{mm}
C4	205 cm^{-1}	14.6	151 cm^{-1}
D5	276 cm^{-1}	5.2	319 cm^{-1}

At high temperatures, the fluorescence from the activator convoluted the lasing transition emission for the sensitizer. The results obtained by linear fits shown in Fig. 12 are tabulated in Table II. The sensitizer column refers to the sensitizer pumped. ΔE_s is the activation energy determined by the slope of the linear fit to Fig. 12 with Eq. 25, and the intercept was identified with the constant $\frac{W_{sa}}{W_{as}}$. ΔE_{mm} is the energy mismatch at 10 K between the metastable states of the sensitizer and activator. Both the activation energy and energy mismatch are higher for site D5 than C4. The actual Stark spliting of the $^4F_{3/2}$ manifold of the sensitizer was not measured.

The explicit mechanism by which energy transfer occurs was intentionally neglected in the rate equation model because (1) it is unclear which specific crystal field sites correspond to sites A2, C4, and D5; and (2) the energy transfer rate occurs in a time regime inaccesible by the experiment. However, the basic characteristics of the energy transfer seem clear. The energy transfer is nonradiative, and involves either dipole-dipole, dipole-quadrupole, or quadrupole-quadrupole resonance. Following the treatment by Forster, [7] [8] [9] Inokuti and Hirayama [10],

the energy transfer rate, W_{sa}, may be described as

$$W_{sa} = \frac{1}{\tau_s} \cdot (\frac{R_0}{R})^m \tag{26}$$

where τ_s is the sensitizer lifetime, R_0 is the critical interaction distance, and R is the distance between the sensitiizer and activator. The exponent m is 6, 8, and 10 for dipole-dipole, dipole-quadrupole, and quadrupole-quadrupole interactions respectively. Experiment shows that the energy transfer must occur on a time scale less than 10 μs (if the time scale of transfer was longer than 10 μs, one would observe a time dependence of the relative integrated intensities of the sensitizer and activator emission). Since the lifetime of the sensitizer is 350 μs and the energy transfer rate must be greater than $\frac{1}{10\mu s} = 10^5$ Hz, Eq. 26 implies the $R_0 > R$. For the dipole-dipole interaction, the maximum ion separation, R_{max}, for this fast transfer rate is related to the critical interaction distance by

$$R_{max} \leq 0.55 R_0 \tag{27}$$

With no knowledge of the actual crystal sites for the sensitizer and activator, the best one can do is estimate ion separation through a homogeneous distribution. The problem with assuming a homogeneous distribution is that not only is it unphysical (the Nd^{3+} ions substitute at specific sites), but Forster's theory was developed for transfer between distinct sites, not distributions of sites. The mean separation between like ions may be determined from

$$D_{mean} = 2 \cdot (\frac{3}{4\pi C})^{\frac{1}{3}} \tag{28}$$

where C is the ion concentration. Assuming that the ion concentration (1×10^{20} cm^{-3}) is equally distributed among the sites A2, C4, and D5, the mean distance between two like ions is 39 Å. Using the critical interaction distance for impurity ions in Nd:YVO_4 [11] of 14 Å as a crude estimate of the critical interaction distance, the sensitizer-activator ion separation must be less than $R_{max} = 8$ Å for fast energy transfer to occur. On average, this ion pair is isolated from the other ions by a distance in larger than R_{max}, so multiple step diffusion among ion pairs is

unlikely. Fast dipole-dipole resonant energy transfer for low sensitizer and activator concentration requires the introduction of isolated sensitizer-activator pairs. The energy transfer is consequently limited by the number of available pairs within the crystal, and by the rate of back transfer.

In conclusion, the energy transfer process between nonequivalent crystal field sites for Nd^{3+} in BMAG has been modeled by thermally activated resonant multipole interaction between the $^4F_{3/2}$ Stark components of the sensitizer and activator. Energy transfer proceeds to a single activator, site A2. Fast energy transfer is postulated between ion pairs. The activation energies determined are consistent with the Stark splitting expected of the sensitizer $^4F_{3/2}$ manifold, and qualitatively follow the energy mismatch. A constant proportional to the forward to back transfer rate ratio was determined.

CHAPTER III

EXCITED STATE ABSORPTION AND LASER SLOPE EFFICIENCIES

Experiment

A Light Age Model 101 PAL alexandrite laser with an output tunable between 725 and 790 nm was used to pump Nd^{3+} in BMAG (Nd:$Ba_2MgGe_2O_7$). The alexandrite laser pulse was 60 μs (FWHM) and the maximum power at the peak of the gain curve of the alexandrite laser was 20 W at a repetition rate of 20 Hz. The spectral width of the laser output was approximately 1 nm.

The fluorescence emission from the sample was sent through a 1-meter monochromator, detected with an RCA C31034 photomultiplier tube, analyzed by a boxcar integrator, and recorded on a chart recorder. A spectral resolution of 1 nm was obtained and the fluorescence was corrected for the response of the filter, grating, and the detector.

Absorption measurements for optical pumping along the $\vec{C}$-axis of the sample were performed upon an IBM UV-Vis-Near IR absorption spectrometer. Absorption spectra were corrected for scattering due to the BMAG host.

For the laser slope efficiency measurements, the crystal was mounted in a 22.5 cm cavity consisting of a 100 % reflector with a 50 cm radius of curvature and a flat 85 % output coupler. Transverse pumping was employed ($\vec{E} \perp \vec{C}$) with cylindrical and convex lenses used to focus the pump laser beam in a line of width 0.02 cm and length (0.56 cm) of the Nd-BMAG sample. An iris was positioned in the cavity to limit the number of oscillating transverse modes and to eliminate lasing due to the sample surface reflections. The power incident on the Nd-BMAG crystal and the power output from the Nd-BMAG laser were measured simultaneously with two calibrated power meters. The fresnel reflections and absorption

within the excited mode volume of the sample were considered when calculating the power absorbed by the crystal.

Spectral Studies of Excited State Absorption

Blue and green fluorescence was observed (by eye) for alexandrite pumping of Nd^{3+} in BMAG over an extended spectral region in the presence and absence of Nd^{3+} lasing at 1054 nm. The intensity of the fluorescence did not significantly increase when the sample was lasing. Lasing was observed for pump wavelengths from 736.7 nm to 758.8 nm, which falls between the beginning and trailing edges of the absorption spectrum shown in Fig. 13. Blue fluorescence was observed for excitation between 728.8 and 751.7 nm and the green fluorescence was detected for excitation in the 746.7 to 770.5 nm region. The blue fluorescence was the most intense at pump wavelengths of 738.2 to 738.6 nm and was clearly visible to the naked eye. The green fluorescence was very dim, and required a red cut-off filter to distinguish it from the intense red alexandrite pump beam. The green fluorescence gradually reduced in intensity from its low wavelength onset until it disappeared at 770.5 nm. The ground state absorption was high for the pump wavelengths resulting in maximum blue emission.

Fluorescence spectra were recorded at pump wavelengths of 738.6, 743.2, and 753.6 nm. The 738.6 nm excitation was chosen because it produced the most intense blue fluorescence. The 753.6 nm excitation was selected because it yielded the greatest laser output power at 1054 nm of all pump wavelengths producing visible green fluorescence, and the pump wavelength of 743.2 nm was selected both for its strong ground state absorption and its predicted resonant excited state absorption of pump photons transition ($^4F_{5/2} + {}^2H_{9/2} \rightarrow {}^2P_{3/2}$). The green fluorescence, although present, was found in no way to diminish the pump wavelength perfomance of the Nd:BMAG laser and is not measured to be a dominant loss process in the material.

Figure 14 is the fluorescence of Nd^{3+} in BMAG over the spectral range 380 to 630 nm. The spectra was corrected for both detector and filter response.

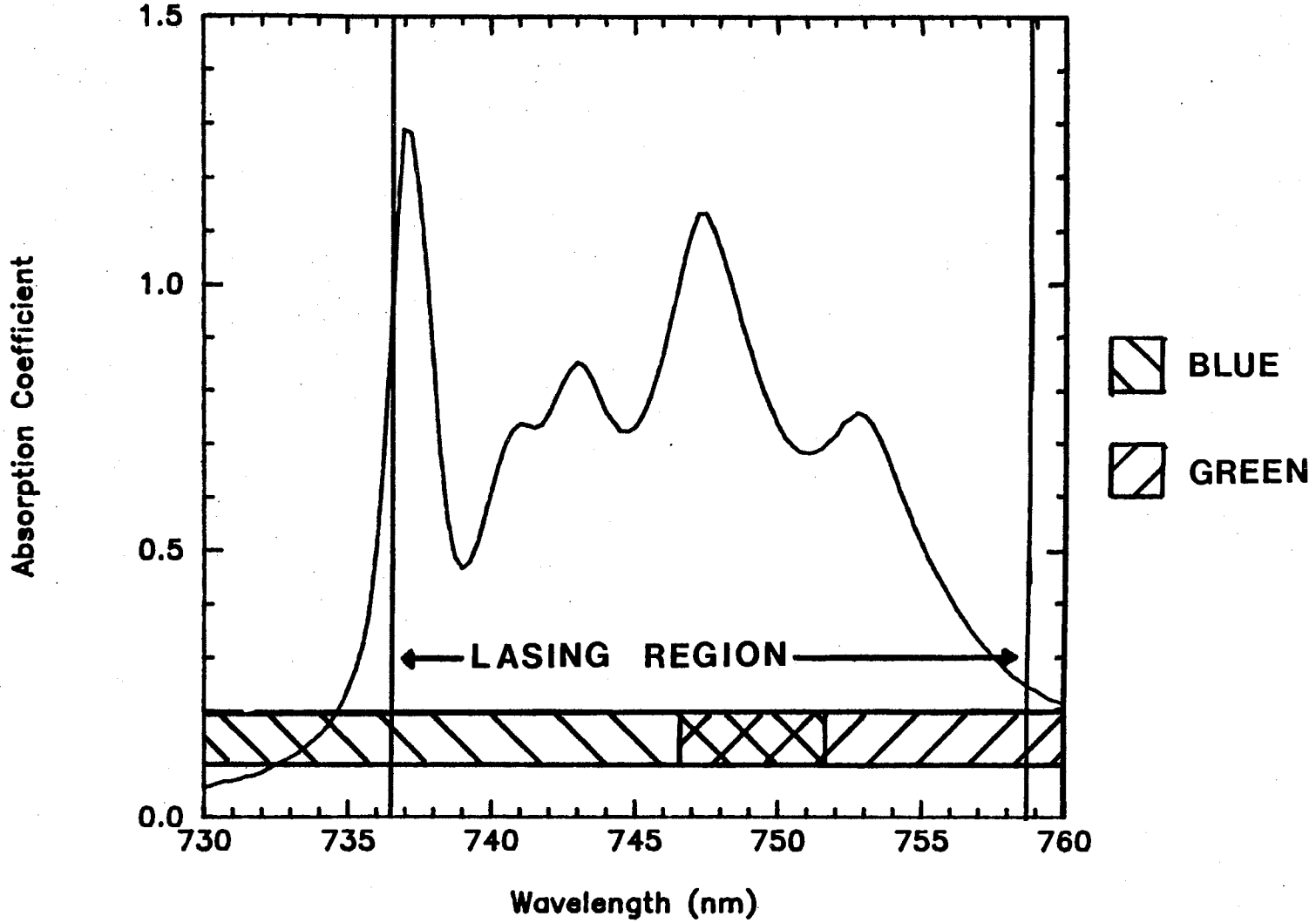

Figure 13. Observed Wavelength Dependence of the Blue and Green Emission Relative to the Room Temperature Absorption Manifold Pumped by the Alexandrite Laser.

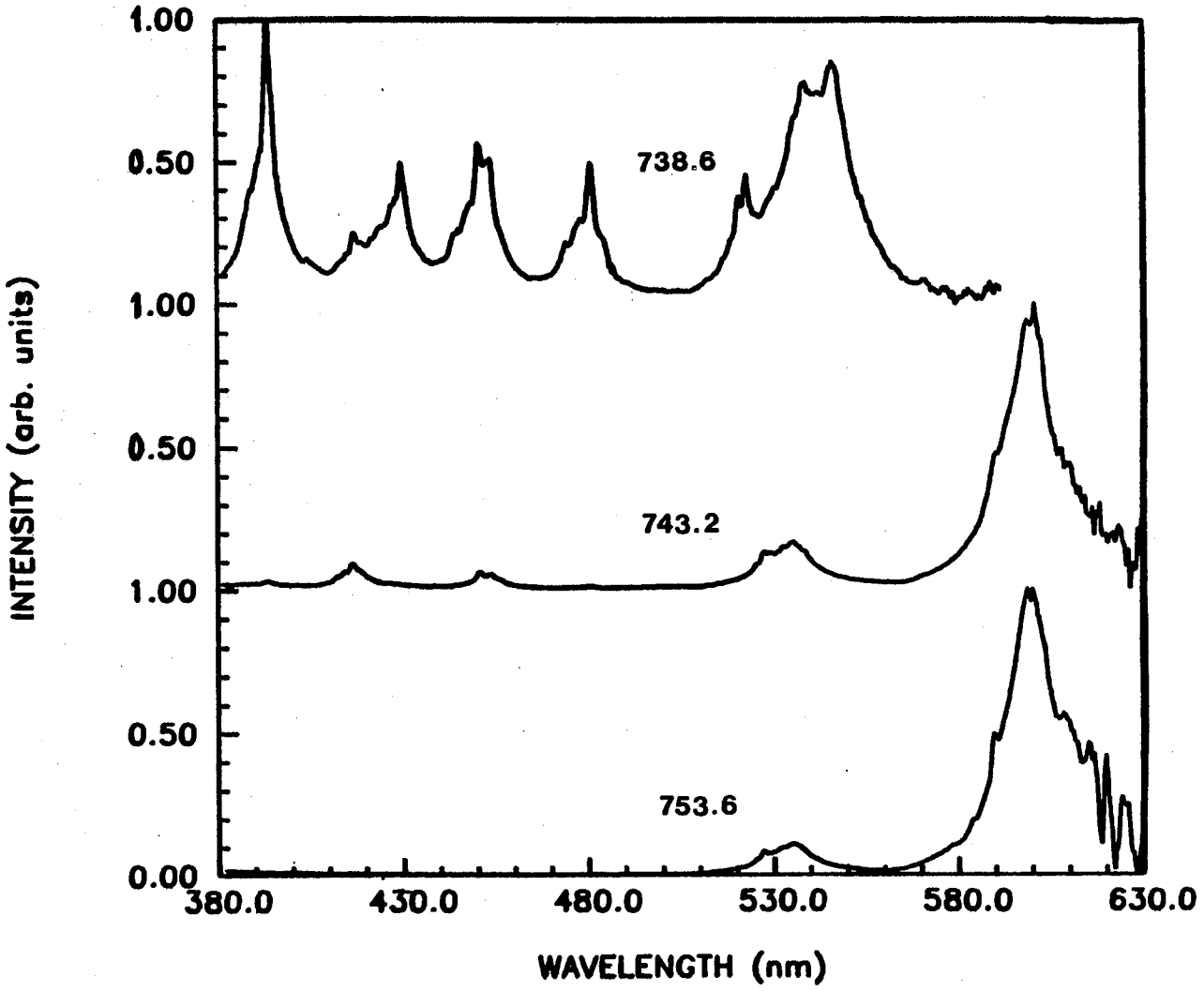

Figure 14. Room Temperature Fluorescence of Nd:BMAG for Different Excitations of the Alexandrite Laser.

Because the transmittance of the cutoff filter zeroes for wavelengths less than 380 nm and greater than 630 nm, the scan region is limited and the correction for filter response introduces artifacts near the wavelength limits. Each spectra was normalized to the highest peak in the scan range. The absolute intensity for the 738.6 nm spectrum (top) is roughly an order of magnitude greater than for the 743.2 and 753.6 nm excitations, in agreement with the qualitative observation of intense blue and weak green fluorescence discussed earlier. The observed emission is tabulated by pump wavelength in Table III.

Comparison of the three spectra reveals that fluorescence which appears "blue" has a series of peaks in the 380 to 500 nm spectral range and the weak "green" spectum has fluorescence peaks at 530 and 600 nm. Transitions between the various Stark manifolds result in the broad, fluorescent groups (e.g. $^4D_{3/2} \rightarrow {}^4I_{9/2}$). The fine structure observed within each broad fluorescent emission band is attributed to transitions between the Stark components of the manifolds (e.g. the $j = \frac{1}{2}$ component of the $^4D_{3/2}$ manifold to the $j = \frac{1}{2}$ component of the $^4I_{9/2}$ manifold).

Modeling the fluorescent emission required knowledge of the energy levels at room temperature. The room temperature energy levels of Nd^{3+} in BMAG were determined from absorption and fluorescence spectra, and are presented in Table IV. The Full Width at Half Maximum (FWHM) of each level was estimated from constructed Gaussian fits to absorption and fluorescence bands. The FWHM of the high energy manifolds is larger than that for the low energy manifolds because the absorption spectrometer resolution is constant in wavelength, and results in greater energy uncertainity at low wavelengths. Two absorption coefficients are reported: (1) the absolute absorption coefficient at the band maximum, α_a, and (2) the absorption coefficient determined from the constructed Gaussian, α_g. Spectroscopic LSJ labels were assigned to each energy level. No attempt was made to separate hot band transitions or to deconvolute the multi-site contributions of Nd^{3+} in BMAG when constructing the energy level diagram.

TABLE III

OBSERVED FLUORESCENCE FOR
ALEXANDRITE PUMPING
OF Nd:BMAG

Pump Wavelength (nm)			Fluorescent
738.6	743.2	753.6	Transition
388-393	385-393	-	6,8
416-429	414-426	-	7,9
441-456	450-457	-	10
473-483	477-480	-	11
520-545	525-534	524-535	12,13
-	589-592	577-596	14

TABLE IV

ROOM TEMPERATURE ENERGY LEVEL PARAMETERS OF Nd:BMAG

Stark Manifold	Peak (cm^{-1})	α_a (cm^{-1})	α_g (cm^{-1})	FWHM (cm^{-1})
$^4D_{7/2}$, $^2I_{13/2}$	30377	0.543	0.070	737
$^4D_{1/2}$	28514	0.790	0.395	342
$^4D_{5/2}$, $^2I_{11/2}$	27964	0.884	0.489	422
$^4D_{3/2}$	27405	0.477	0.082	286
$^2P_{3/2}$	26788	0.424	0.008	108
	26504	0.411	0.008	112
	26110	0.411	0.014	212
	25826	0.399	0.010	147
$^2D_{5/2}$	23776	0.337	0.008	266
$^2P_{1/2}$	23218	0.354	0.029	129
	23010	0.366	0.041	243
$^4G_{11/2}$	22026	0.333	0.012	141
	21763	0.358	0.033	142
	21622	0.358	0.037	164
$^2D_{3/2}$	21182	0.382	0.062	216
$^4G_{9/2}$	20995	0.395	0.074	185
$^2G_{9/2}$	19569	0.613	0.099	84
	19478	0.691	0.103	83
	19353	0.625	0.111	86

TABLE IV (Continued)

Stark Manifold	Peak (cm^{-1})	α_a (cm^{-1})	α_g (cm^{-1})	FWHM (cm^{-1})
$^4G_{7/2}$	19030	1.020	0.300	145
	18868	0.687	0.095	78
	18761	0.629	0.091	92
$^4G_{5/2}$,	17501	1.200	0.391	75
$^2G_{7/2}$	17483	0.851	0.411	83
	17209	1.300	0.440	92
	17103	1.440	0.370	73
	17030	1.680	0.387	58
	16972	1.520	0.325	55
	16846	1.090	0.280	105
	16711	0.802	0.391	87
$^2H_{11/2}$	16271	0.321	0.008	50
	16171	0.329	0.017	78
	16067	0.321	0.012	57
	15946	0.313	0.008	84
$^4F_{9/2}$	14550	0.387	0.058	188
	14409	0.370	0.012	73
	14296	0.366	0.041	135
$^4F_{7/2}$,	13567	1.380	0.971	50
$^4S_{3/2}$	13460	1.200	0.560	73
	13382	1.470	0.596	59
	13289	1.130	0.494	62
	13154	0.559	0.140	73
$^4F_{5/2}$,	12750	0.382	0.054	44
$^2H_{9/2}$	12679	0.485	0.095	40
	12553	0.929	0.341	35
	12505	1.170	0.395	39
	12429	2.040	1.150	42
	12334	0.880	0.288	52
	12252	0.621	0.136	50

TABLE IV (Continued)

Stark Manifold	Peak (cm^{-1})	α_a (cm^{-1})	α_g (cm^{-1})	FWHM (cm^{-1})
$^4F_{3/2}$	11533	0.572	0.189	52
	11399	1.070	0.600	49
	11307	0.588	0.132	47
	11191	0.428	0.078	84
	11046	0.325	0.029	68
$^4I_{15/2}$	6242	0.169	0.025	64
	6156	0.154	0.012	47
	6062	0.156	0.014	69
	5961	0.154	0.010	48
$^4I_{13/2}$	4359	0.160	0.017	35
	4278	0.177	0.035	51
	4225	0.193	0.049	34
	4170	0.284	0.070	77
	4102	0.251	0.054	27
	4057	0.280	0.070	35
	4017	0.226	0.078	38
$^4I_{11/2}$	2176			67
	2093			74
	2029			76
	1933			47
$^4I_{9/2}$	683			78
	364			101
	235			97
	102			96
	0			70

The blue and green emission observed for alexandrite pumping of Nd:BMAG is modeled by Excited State Absorption (ESA). ESA occurs for alexandrite pumping because the peak power over the 60 μs pulse is 16 kW, more than ample power to excite every Nd^{3+} within the excitation volume of the sample. ESA involves the absorption of a second photon by an optically excited ion. The excited states from which ESA occurs must be populated and have decay rates (inversely proportional to the level lifetime) less than or equal to the photon rate inducing absorption. The probability of any ion undergoing an ESA transition therefore is proportional to the ratio of excited to ground state ions. As pump powers reach and exceed the saturation limit, the excited to ground state ion ratio increases to the point where ESA becomes likely.

Excited state absorption may be classified according to the type of photon that is absorbed: ESA of lasing photons and ESA of pump photons. ESA of sample emission in Nd:BMAG only is probable for self absorption of the 1054 nm lasing photons. The reason for this is (1) the flux of lasing photons in the mode volume of the laser cavity is high; (2) the highly populated $^4F_{3/2}$ metastable state is separated from $^4G_{9/2}$ by an energy gap equal to the lasing photon energy; and (3) the transition is spin allowed. ESA of lasing photons by electrons in other manifolds not only has to compete with fast nonradiative decays but also is nonresonant. So the only ESA of lasing photons process considered for alexandrite pumping of Nd:BMAG is the resonant self absorption of the 1054 nm lasing photons for the transition $^4F_{3/2} \rightarrow {}^4G_{9/2}$.

The important distinction between ESA of pump and lasing photons is resonance. In ESA of pump photons, the energy of the photon to be absorbed may be varied by changing the excitation wavelength. When the pump photon energy equals the energy gap between two excited states, resonant absorption is possible. Phonon assisted absorption is also possible for energy mismatch within $\pm \approx 200$ cm^{-1} (typical phonon energies in the BMAG host). ESA of pump photons, therefore, may be tuned by varying the excitation wavelength. For ESA of the

lasing photons no such tuning is possible, because the lasing wavelength is independent of pump wavelength. The fluorescence in Fig. 14 depends dramatically upon pump wavelength, indicating that ESA of the alexandrite pump photons an active process in the material.

Three resonant ESA of pump photons transitions are proposed in addition to self absorption of lasing photons to explain the fluorescence observed in Fig. 14. Figure 15 shows these transitions with respect to the room temperature energy level diagram for Nd:BMAG. Spectroscopic manifold labels appear beside the emperically determined energy levels of Nd^{3+} in BMAG. Transition (1) represents ground state absorption of the alexandrite pump photons. Transition (2) is resonant ESA of the 1054 nm lasing photons. Transitions (3) - (5) are resonant ESA of pump photon transitions. Transitions (6) - (14) are predicted radiative transitions from states populated by ESA. Only the transitions which result in fluorescence within the scan range of the experiment (380 - 630 nm) are illustrated in Fig. 15. The fluorescence transition numbers in Fig. 15 also correspond to the fluorescent transition numbers found in Table III. Using the empirical room temperature energy levels it was possible to estimate the wavelength ranges of the fluorescent transitions marked in Fig. 15. These predicted emission wavelengths are tabulated in Table V.

Examination of Table V reveals that emission from the $^4D_{3/2}$ and the $^2P_{3/2}$ manifolds is the "blue" fluorescence, and the "green" fluorescence is due to emission from the $^4G_{9/2}$ and $^4G_{7/2}$ manifolds. ESA transitions (4) and (5) are proposed to populate the $^2P_{3/2}$ and $^4D_{3/2}$ manifolds respectively. Transition (5) is only resonant from the highest level in the pump manifold. Transition (4) is believed to come from the $^2H_{9/2}$ rather than the $^4F_{5/2}$ because doublet-doublet transitions are spin allowed.

Figure 16 represents the pump regions for resonant ESA of pump photons. Figure 16 was constructed by treating the Stark manifolds as Gaussian distributions with the FWHM determined from the lowest and highest lying energy levels in the manifold. In this construction, the pump wavelength for maximum resonant

TABLE V

FLUORESCENT TRANSITIONS PREDICTED
FROM THE ROOM TEMPERATURE
ENERGY LEVELS OF
Nd:BMAG

Initial Level	Final Level $^4I_{9/2}$	$^4I_{11/2}$	$^4I_{13/2}$
$^4D_{3/2}$	365-374 nm	392-397 nm	428-434 nm
$^2P_{3/2}$	383-393 nm	413-417 nm	453-460 nm
$^4G_{9/2}$	476-492 nm	525-531 nm	589-601 nm
$^4G_{7/2}$	533-553 nm	594-603 nm	678-694 nm

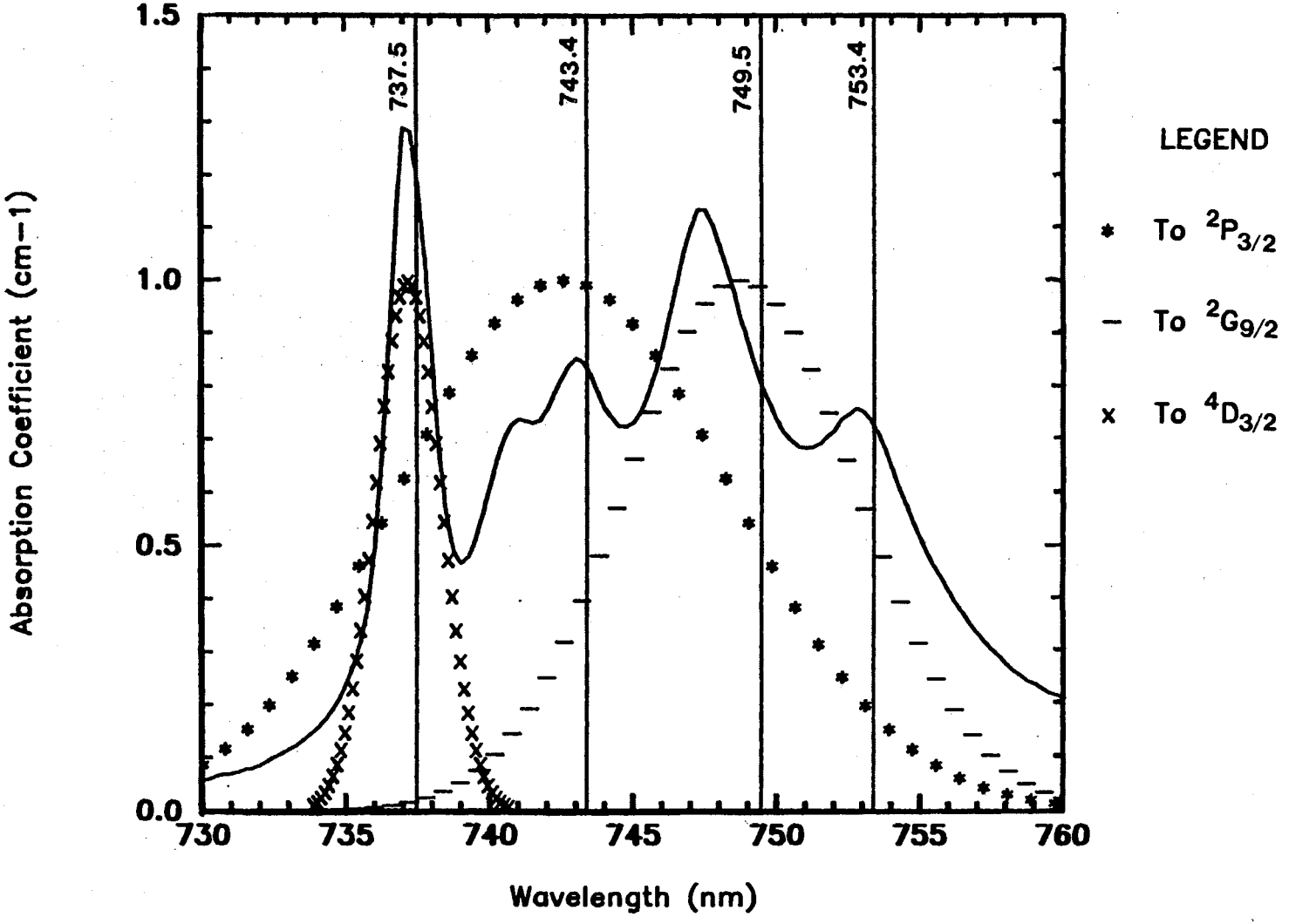

Figure 16. Theoretical Construction for the Pump Wavelength Dependence of Excited State Absorption.

ESA corresponds to the manifold center to manifold center energy gap, or the peak separation of the two constructed Gaussians. The overlap of the two Gaussians was determined about the center resonant wavelength, and the normalized curve was superimposed upon the absorption spectrum. The height of the three ESA resonance curves was normalized because the absorption cross sections for the three transitions are unknown. Although crude, this construction qualitatively predicts the pump wavelength dependence of the observed blue and green fluorescence remarkably well. ESA into $^2G_{9/2}$ and subsequent green emission from $^4G_{7/2}$ are resonant for higher pump wavelengths than ESA resulting in blue emission. The maximum blue emission observed for 738.2 - 738.6 nm pumping lies in the crossover region where absorption into both $^2P_{3/2}$ and $^4D_{3/2}$ is possible. Blue-green fluorescence observed for pump wavelengths 746.7 to 751.7 nm lies in the region where both ESA to $^2P_{3/2}$ and $^2G_{9/2}$ is possible.

Returning to Fig. 14 with a qualitative understanding of Fig. 16, one sees that excitation at 738.6 nm results in excited state absorption to and fluorescent emission from both the $^2P_{3/2}$ and $^4D_{3/2}$ manifolds. The agreement between the observed and predicted fluorescence in Tables III and V for these manifolds is good. The emission from $^4D_{3/2}$ is more intense than that of $^2P_{3/2}$ because the latter is spin forbidden to the ^4I states. Note that the absorption coefficient for $^4D_{3/2}$ is roughly an order of magnitude larger than that for $^2P_{3/2}$. The probability of spontaneous emission from an excited state may be related to the absorption coefficient. Following the treatment of Siegman [6], the growth and decay for a wave passing through an absorbing or amplifying medium may be described by

$$I(z) = I(z_0)e^{-2\alpha_m(z-z_0)} \tag{29}$$

Comparison of Eq. 29 with Beer's law (equation 56 discussed later) reveals

$$\alpha = 2\alpha_m \tag{30}$$

where α is the ground state absorption coefficient. Absorption coefficient is related to the stimulated emission cross section by

$$\alpha = 2\alpha_m = \Delta N_{12}\sigma_{21} \tag{31}$$

where

$$\Delta N_{12} = \frac{g_2}{g_1} N_1 - N_2 \tag{32}$$

and N_1, N_2 are the density of ions in the ground and excited states, g_1 and g_2 are the degeneracies of the two states, and σ_{21} is the stimulated emission cross section. For ground state absorption measurements, the population in the ground state is much larger than that of the excited state, so Eq. 31 may be written as

$$\sigma_{21} = \frac{g_1}{g_2} \frac{\alpha}{N_1} \tag{33}$$

The general relation between stimulated absorption and emission cross sections as reported by Siegman is

$$\sigma_{ji}(w_a) = (\frac{g_i}{g_j})\sigma_{ij}(w_a) = \frac{3^*}{2\pi} \frac{\gamma_{rad,ji}}{\Delta w_a} \lambda_{ij}^2 \tag{34}$$

where 3^* is a dimensionless polarization overlap factor for atomic transitions, w_a is the atomic transition frequency, Δw_a is the atomic linewidth (FWHM) in radians/sec, $\gamma_{rad,ji}$ is the radiative decay rate from j to i, and λ_{ij}^2 is the transition wavelength in the medium. Since the radiative decay rate is equal to the Einstein A-coefficient, Eq. 34 may be solved in terms of the Einstein-A coefficient

$$A = \frac{2\pi \Delta w_a}{3^* \lambda^2 N_g} \alpha \tag{35}$$

Where A is the Einstein A-coefficient, N_g is the ion concentration, and λ is the transition wavelength. According to Svelto [12], the Einstein A-coefficient may be thought of as the spontaneous emission probability, and is related to the matrix element of the electric dipole moment and spontaneous lifetime (τ_{sp}) by

$$A = \frac{1}{\tau_{sp}} = C w_0^3 |\mu|^2 \tag{36}$$

where w_0 is the atomic transition frequency in free space and the constant C is

$$C \equiv \frac{2n}{3\pi h \epsilon_0 c_0^3} \tag{37}$$

where n is the index of refraction, h is Planck's constant, ϵ_0 is the permittivity of free space, and c_0 is the speed of light *in vacuo*. The quantity $|\mu|^2$ may be determined from the magnitude of the matrix element of the electric dipole moment,

$\vec{\mu_{if}}$,

$$\vec{\mu_{if}} = e \int u_f^* \vec{r} u_i d\tau \tag{38}$$

where e is the electronic charge, u_i and u_f are the atomic wavefunctions of the initial and final states, and $\vec{r}$ is the position vector of the electron undergoing the transition. The point of the entire preceeding argument is to demonstrate that the absorption coefficient is directly proportional to the probability of spontaneous emission from the excited state (Eq. 35). Excited states with larger absorption coefficients, consequently have higher emission intensities to the ground state. The selection rules arise from the zeroing of the matrix of the electric dipole moment from parity considerations [13] (the integral of a function of odd parity over symmetric limits is identically zero; $\vec{r}$ is of odd parity; the parity of the atomic wavefuntions is determined by the angular momentum; if the initial and final atomic wavefunctions have the same parity, then the parity of the integrand is odd and the matrix element zeroes). According to Eisberg and Resnick [13], the spin selection rule for atoms with several optically active electrons (e.g. Nd^{3+}) having total spin angular momentum, s, is

$$\Delta s = 0 \tag{39}$$

so quartet-doublet transitions are spin forbidden. However, mixing of the atomic wavefunctions occurs when the ion is placed in a host with a crystal field, so spin is not a good quantum number, and strictly spin forbidden transitions occur. The transition strength of spin forbidden transitions is much weaker than spin allowed transitions in rare earth doped materials because the optically active 4f electrons are partially shielded by outer shell electrons from the crystal field of the host. This shielding reduces the influence of the crystal field, so the wavefunctions describing the 4f states retain much of the character of the free ion wavefunctions. So the spin selection rule, although not absolutely followed, is a good indicator of relative transition strengths.

Table IV shows that the absorption coefficients in general are higher for the quartet states than the doublet states, indicating that spin forbidden transitions in BMAG are weaker than spin allowed transitions. As the excitation wavelength

is changed from 738.6 nm (resonant ESA to $^4D_{3/2}$) to 743.2 nm (resonant ESA to $^2P_{3/2}$) the absolute intensity drops an order of magnitude. Because the blue emission is more intense for $^4D_{3/2}$, the brightest blue observed depends strongly upon $^4D_{3/2}$ resonance. Blue emission in Nd:YAG is much weaker than that for BMAG [14], and may be due to an absence of $^4D_{3/2}$ resonance.

The emission at 480 nm in Fig. 14 is largest for excitation at 738.6, very weak at 743.2 nm, and absent at 753.6 nm. The 480 nm emission is characteristic of $^4G_{9/2} \rightarrow {}^4I_{9/2}$. If ESA of lasing photons was a dominant process in Nd:BMAG, one would expect strong 480 nm emission independent of pump wavelength, since the $^4G_{9/2}$ manifold is populated by this mechanism. The excitation wavelength dependence of the 480 nm emission in the fluorescence spectra, and the complete absence of 480 nm emission at 753.6 nm excitation infers that ESA of the alexandrite pump photons is the dominant process responsible for the green emission in Nd:BMAG. ESA of lasing photons is not ruled out, it just is not responsible for the green fluorescence observed in Fig. 14.

The green fluorescence at 530 and 600 nm is characteristic of emission from $^4G_{7/2}$ to $^4I_{9/2}$ and $^4I_{11/2}$ (see Table V). The only resonant excited state absorption of pump photons transition that populates $^4G_{7/2}$ for alexandrite pumping from 730 -760 nm is $^4I_{15/2} \rightarrow {}^2G_{9/2}$ (transition (3) in figure 15). This transition explains the very weak, pump wavelength dependent green fluorescence. Because the energy gap between $^2G_{9/2}$ and $^4G_{7/2}$ is roughly 600 cm^{-1}, electrons in $^2G_{9/2}$ primarily nonradiatively relax into $^4G_{7/2}$. Figure 16 predicts that 753.6 nm pumping results primarily in ESA to $^2G_{9/2}$, and agrees with the fluorescence in Fig. 14.

At 738.6 nm, the pump photons are no longer resonant with $^2G_{9/2}$ (see Fig. 16). The $^4G_{9/2}$ manifold is populated by the electrons which nonradiativly decay out of $^4D_{3/2}$ and $^2P_{3/2}$, resulting in strong emission to $^4I_{9/2}$ and $^4I_{11/2}$ (480 and 530 nm). At 743.2 nm, $^4G_{9/2}$ is populated by nonradiative decay from $^2P_{3/2}$. Because the excited state absorption is weaker at 743.2 nm, fewer electrons nonradiatively relax, and the $^4G_{9/2}$ emission is reduced. Figure 16 predicts that ESA to $^2G_{9/2}$

is possible. Because the $^4G_{9/2}$ emission is so weak (notice the weak signal at 480 nm), the 530 nm fluorescence is due primarily to ESA to $^2G_{9/2}$.

At first glance, the ESA transition proposed for green emision may seem unphysical. The branching ratio for many Nd-doped materials indicates less than one percent of excited ions decay to $^4I_{15/2}$ from the $^4F_{3/2}$ metastable level. With a fluorescent lifetime of 350 μs, only ten percent of $^4F_{3/2}$ ions decay during the 60 μs alexandrite pulse duration. This gives a total of less than a tenth of a percent of the excited population in $^4I_{15/2}$ during the alexandrite laser pulse. It seems unlikely that excited state absorption would occur from a state with so few excited ions. However, one must recall that the pump powers used reach and exceed that for absorption saturation for alexandrite pumping, and the population in this manifold is not negligable over the 60 μs alexandrite pulse duration. If the ^4I ground state absorption is any indicator of the ESA cross section from $^4I_{15/2}$ to $^2G_{9/2}$, then the ESA cross section should be higher than that for $^4D_{3/2}$ because the absorption coefficient is higher (see Table IV). As derived earlier, the spontaneous emission rate is proportional to the ground state absorption coefficient, so the relative emission rate to the ground state from $^4G_{7/2}$ should be higher than that from $^4D_{3/2}$ and $^2P_{3/2}$ because the absorption coefficient is higher (0.3 verses 0.08 and 0.01 cm^{-1}). The energy gap to the next lowest manifold is $\approx$ 2000 cm^{-1} for $^4I_{15/2}$ verses $\approx$ 1000 cm^{-1} for ($^4F_{7/2}$+$^4S_{3/2}$) and ($^4F_{5/2}$+$^2H_{9/2}$) the initial states for ESA to $^4D_{3/2}$ and $^2P_{3/2}$. The large energy gap for $^4I_{15/2}$ causes nonradiative leakage to lower states to proceed at a rate slower than that for the other two ESA initial states, so the population that does reach $^4I_{15/2}$ stays there longer. Considering (1) the longer lifetime of $^4I_{15/2}$, (2) the higher absorption coefficient for $^4I \rightarrow {}^2G$, (3) the agreement between the predicted resonance response in Fig. 16 with the observed resonant response in Fig. 13, (4) the absence of $^4G_{9/2}$ emission for 753.6 nm pumping, (5) the relatively high spontaneous emission rate for $^4G_{7/2}$, and (6) pump powers exceeding absorption saturation, it seems indeed possible that ESA of alexandrite pump photons from $^4I_{15/2} \rightarrow {}^2G_{9/2}$ is responsible for the very weak green emission. It is important, however, to realize that this ESA transition was

measured to have little or no bearing upon the laser performance of the material, and is only proposed to explain the observed green fluorescence.

To briefly summarize, ESA of pump photons has been proposed to explain the blue and green emission observed for alexandrite pumping of Nd:BMAG. The blue emission is due to ESA to $^4D_{3/2}$ and $^2P_{3/2}$. The most intense blue is due to emission from $^4D_{3/2}$, and occurs for excitation into the highest energy level in the $^4F_{7/2} +^4 S_{3/2}$ pump manifold. ESA to $^2P_{1/2}$ occurs for excitation into the higher energy levels of the pump manifold. The weaker green fluorescence is due to ESA to $^2G_{9/2}$ and occurs for excitation into the lower energy levels of the pump manifold. ESA of lasing photons, if not absent, was determined to be weak.

Theory of Excited State Absorption

A theory describing the effect of excited state absorption of pump photons upon the slope efficiency of monochromatically pumped laser materials recently has been developed by M.L. Kliewer and R.C. Powell [14]. The theory involves the steady state solution to a six level rate equation model. The slope efficiency, as defined by the above authors, is the slope of the curve obtained by plotting laser output power versus power absorbed by the pump manifold. The theory was applied to alexandrite pumped Nd:YAG, and the ESA transition $^2H_{9/2} \rightarrow {}^2P_{3/2}$ was proposed as a loss mechanism for 754 nm pumping. Excited state absorption of pump photons is considered to be a loss for absorption from the pump level, the $^4F_{3/2}$ metastable state, and all the energy levels between these two levels. The relation between absorbed power and laser output power in this theory may be described by

$$P_{out} = \eta_s^0 \cdot (1 - \eta_{esa}) \cdot P_a + P_{int} \tag{40}$$

where P_{out} is the laser power output, η_s^0 is the slope efficiency without ESA, η_{esa} is the excited state absorption efficiency, P_a is the power absorbed in populating the pump level (determined from Beer's law), and P_{int} is an intercept power (related to the threshold power). A general expression was reported for η_{esa} along with several simplified cases. Three cases are pertinent to ESA in Nd:BMAG:

Case (1) : No ESA of pump photons

$$\eta_{esa} = 0 \tag{41}$$

Case (2) : $\sigma_5 \neq 0$ $({}^4F_{7/2} + {}^4S_{3/2} \rightarrow {}^4D_{3/2})$

$$\eta_{esa} = \frac{1}{1 + \frac{\sigma_p}{\sigma_5} + \frac{\beta_5}{I\sigma_5}} \tag{42}$$

Case (3) : $\sigma_4 \neq 0$ $({}^4F_{5/2} + {}^2H_{9/2} \rightarrow {}^2P_{3/2})$

$$\eta_{esa} = \frac{1}{1 + (\frac{\beta_4}{\beta_5})(\frac{\sigma_p}{\sigma_4}) + \frac{\beta_4}{I\sigma_4} + \frac{I\sigma_p}{\beta_5}} \tag{43}$$

where the subscript "5" refers to the $({}^4F_{7/2} + {}^4S_{3/2})$ pump manifold, "4" refers to the $({}^4F_{5/2} + {}^2H_{9/2})$ manifold, σ_p is the pump level absorption cross section, I is the peak intensity of the alexandrite laser pulse incident in the mode volume of the laser cavity, σ_5 and σ_4 are the excited state absorption cross sections for absorption from manifolds "4" and "5", and β_4 and β_5 are the nonradiative relaxation rates to the ${}^4F_{3/2}$ and "4" manifolds. With a few substitutions, cases (2) and (3) may be simplified as

Case (2)

$$\eta_{esa} = \frac{1}{1 + A + \frac{B}{P_a}} \tag{44}$$

where

$$A \equiv \frac{\sigma_p}{\sigma_5} \tag{45}$$

$$B \equiv \frac{\beta_5}{f\sigma_5} \tag{46}$$

Case (3)

$$\eta_{esa} = \frac{1}{(\frac{1}{P_a} + C)(P_a + D)} \tag{47}$$

where

$$C \equiv \frac{f\sigma_p}{\beta_5} \tag{48}$$

$$D \equiv \frac{\beta_4}{f\sigma_4} \tag{49}$$

where f is a constant relating the peak intensity, I, and the power absorbed.

$$I = fP_a \tag{50}$$

With these substitutions, the functions relating P_{int} and the threshold power, P_{thr}, for the three cases are:

Case (1)

$$P_{int} = -\eta_s^0 \cdot P_{thr} \tag{51}$$

Case (2)

$$P_{int} = -\eta_s^0 \cdot P_{thr} \cdot (1 - \frac{1}{1 + A + \frac{B}{P_{thr}}}) \tag{52}$$

Case (3)

$$P_{int} = -\eta_s^0 \cdot P_{thr} \cdot (1 - \frac{1}{(\frac{1}{P_{thr}} + C)(P_{thr} + D)}) \tag{53}$$

Inspection of Eqs. 44 and 47 reveal that the excited state absorption efficiency is power dependent. Substituting the results for η_{esa} and P_{int} into Eq. 40 gives an explicit functional form that may be used to fit the output power versus absorbed power curves obtained in efficiency measurements. Because η_{esa} is power dependent, excited state absorption cross sections are better parameters to quantify the ESA at a paticular pump wavelength. For cases (2) and (3), these may be determined from:

Case (2)

$$\sigma_5 = \frac{\sigma_p}{A} \tag{54}$$

Case (3)

$$\sigma_4 = (\frac{\sigma_p}{CD})(\frac{\beta_4}{\beta_5}) \tag{55}$$

with constants A, B, C, and D treated as fitting parameters.

Laser Slope Efficiencies

Figure 17 is data obtained from the slope efficiency experiment for several different pump wavelengths. Laser output power at 1054 nm is plotted versus the average power incident upon the excited mode volume of the sample. The incident power was corrected for losses due to fresnel reflections by using the index of refraction for Nd:BZAG [2]. The data marked "blue max." is that for which the blue emission visible to the eye was brightest. The "green max." corresponds to

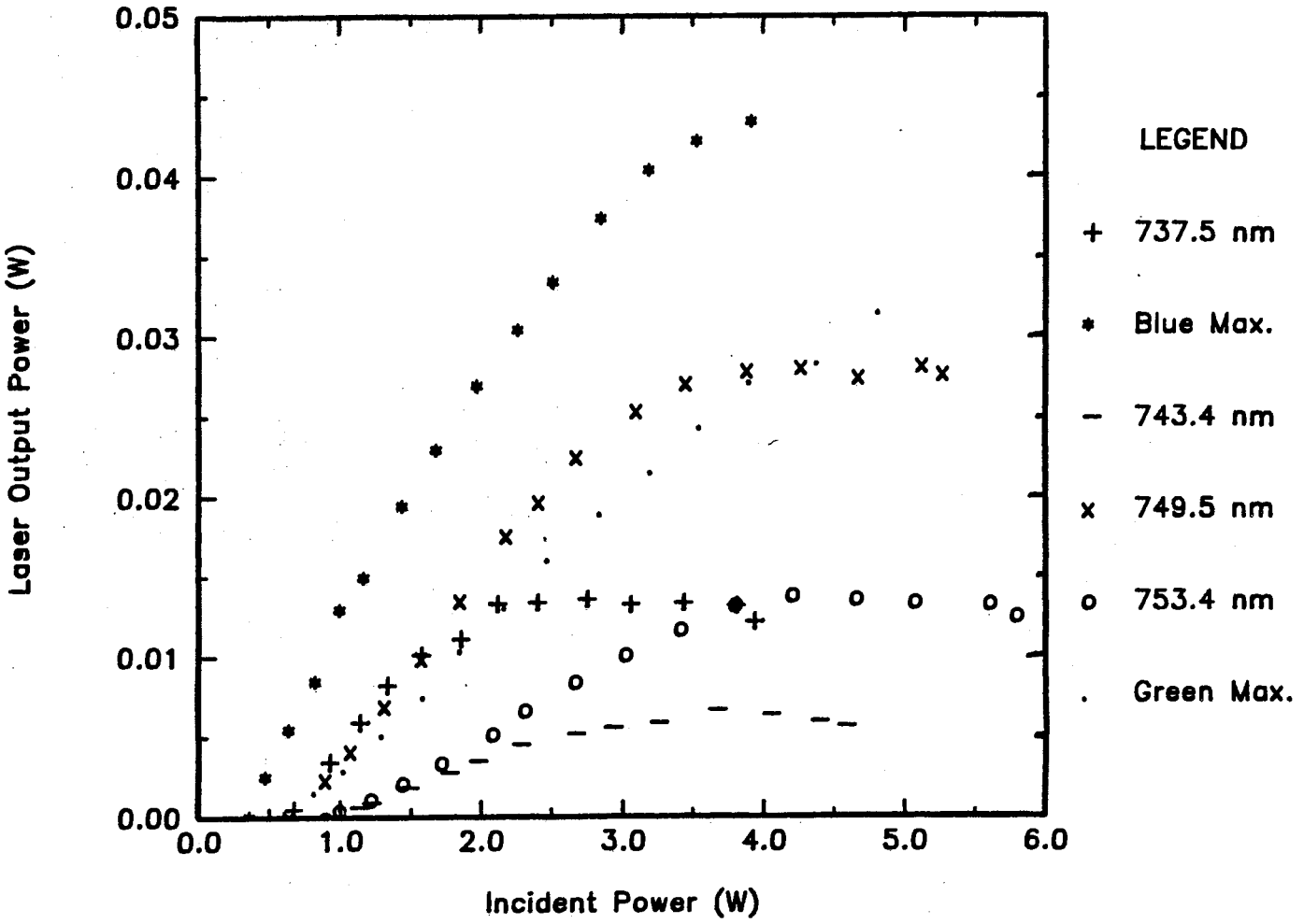

Figure 17. Laser Output Power (1054 nm) Verses Incident Power in the Mode Volume of the Laser Cavity for Different Pump Wavelengths.

cc

the pump wavelength for which the highest laser output power was achieved while the sample emitted green light.

The data in Fig. 17 has not been corrected for the sample's absorption coefficient, so high output power corresponds to regions of high absorption. Although the pump wavelengths for the green and blue maxima were not recorded, the high output power for the blue maximum together with the ESA resonance curve for $^4D_{3/2}$ (see Fig. 16) suggest that the pump wavelength associated with the "blue max." lies in the region 735 to 740 nm.

All of the data in Fig. 17 saturates and curves downward for high incident intensities. Beer's law may be written as

$$I = I_0 e^{-\alpha d} \tag{56}$$

where I is the intensity at a penetration depth d, I_0 is the intensity at the surface of the sample, and α is the absorption coefficient at the pump wavelength. Similarly, the relation between the absorbed power, P_a, and the incident power, P_i, may be determined by

$$P_a = P_i e^{-\alpha d} \tag{57}$$

Ideally, to avoid plotting one dependent variable versus another, one would like to directly measure the absorbed power rather than calculate the power absorbed from Beer's law. The problem with this approach is that the power absorbed used in slope efficiency plots is the power absorbed into the excited mode volume of the cavity. Since the mode volume is small (the calculated cylinder diameter for the cavity used in this experiment is 0.0676 cm), measurement of power reduction across the mode volume of the sample requires very thin samples. Since the thickness of the sample was much greater than the mode volume diameter, it was necessary to calculate the absorbed power from equation 57.

The absorbed power correction was very sensitive to the choice of mode volume diameter. Initial slope efficiency plots using d = 0.0676 cm showed that the downward curvature observed in Fig. 17 occured at roughly the same absorbed

power. Absorption saturation was postulated as the explanation for downward curvature. A calculation based upon one photon absorbed per ion in the mode volume showed complete saturation occurs at 0.11 W absorbed power (using d=0.0676 cm). Good agreement between turnover for all pump wavelengths was achieved for d = 0.0691 cm. The saturation power, P_{sat} = 0.146 W, calculated with the larger diameter agreed better with the onset of curvature observed in the slope efficiency plots. This effective d was adopted as the mode volume diameter for all subsequent calculations becauses of the observed self-consistency and because it was within the error bars of the original calculation.

Figure 18 is the slope efficiency data plotted versus the absorbed power in the mode volume of the laser cavity. The absorbed power correction using Beer's law only applies for absorbed powers less than saturation at 0.15 W. The data is fit with the ESA theory developed earlier. Pumping at 749.5 nm results in the highest slope and the lowest threshold, and is associated with no excited state absorption (Case (1)). Pumping at 737.5 nm results in excited state absorption to $^4D_{3/2}$ (Case (2)). Pumping at either 753.4 or 743.4 results in ESA to $^2P_{3/2}$ (Case (3)). The lowest slope efficiency and highest threshold was observed for 743.4 nm pumping.

The fitting parameters that were the same for each pump wavelength are summarized in Table VI, and the parameters that changed for pump wavelength are tabulated in Table VII. In Table VI, ρ is the approximate ion concentration, V_{ex} is the fraction of the mode volume in the sample excited by the laser pulse, λ_0 is the lasing wavelength, and n is the index of refraction for Nd:BZAG. The slope efficiency without excited state absorption, η_s^0, when treated as a free parameter ranges from 0.26 to 0.29. Twenty six percent was selected as η_s^0 because it deviated least from the highest slope efficiency observed. Because there is ESA throughout the pump multiplet, it is impossible to measure the η_s^0 directly. Case (1) applies for 749.5 nm pumping because the slope efficiency, η_s (calculated from the linear, low power regions of each plot), and η_s^0 agree within the absolute error of the experiment.

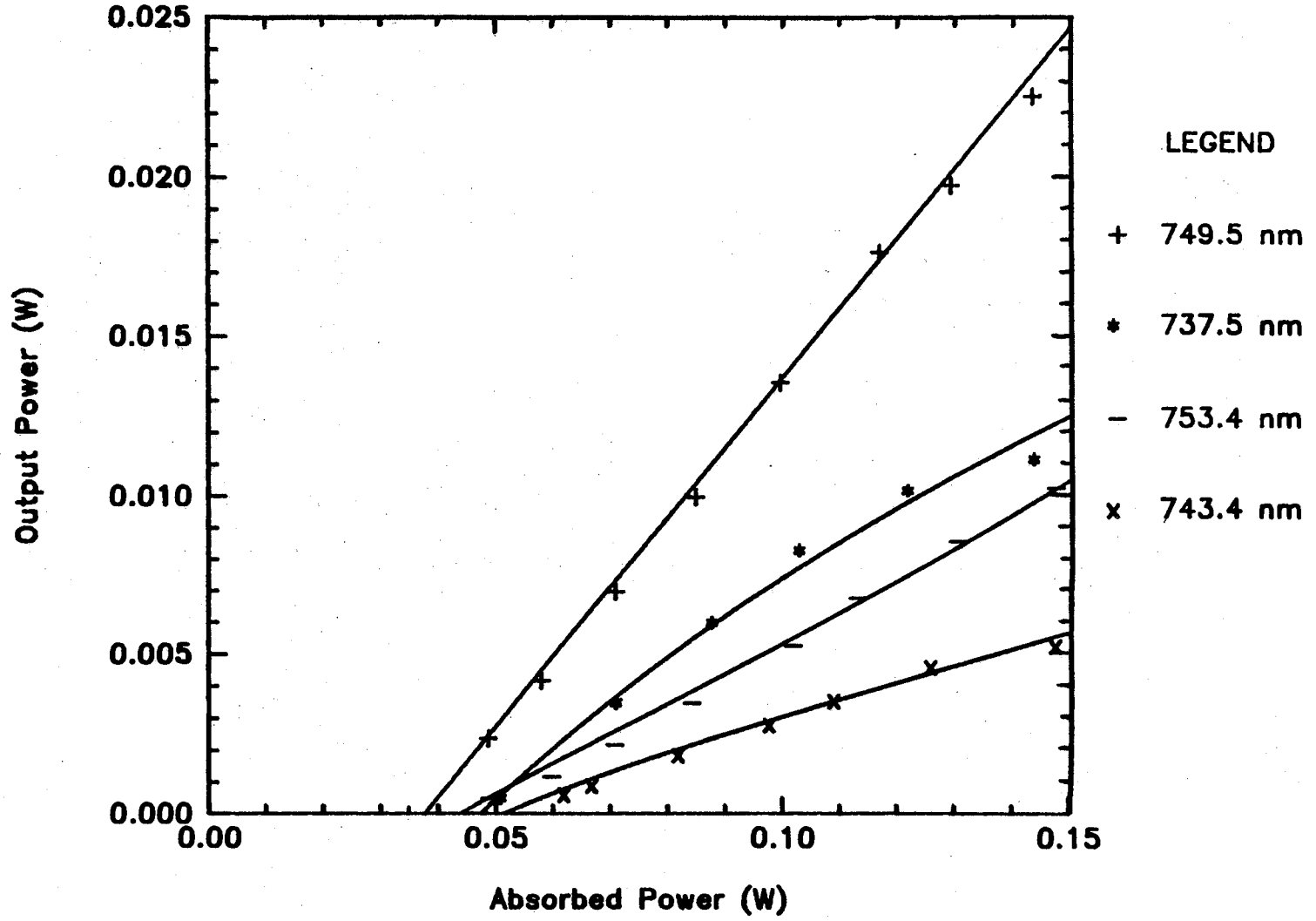

Figure 18. Laser Slope Efficiency Data Fit to ESA Theory.

TABLE VI

PARAMETERS USED TO FIT THE ESA THEORY TO THE SLOPE EFFICIENCY DATA

Parameter	Value
η_s^0	0.26
β_4 (Hz)	4.3×10^6
β_5 (Hz)	3.5×10^6
d (cm)	0.06906
ρ (cm^{-3})	1×10^{20}
V_{ex} (cm^3)	3.8×10^{-4}
P_{sat} (W)	0.146
λ_0 (nm)	1054
n	1.75

TABLE VII

PARAMETERS USED AND OBTAINED FROM THE FITS OF THE ESA THEORY TO THE SLOPE EFFICIENCY DATA

Parameter	Pump Wavelength (nm)			
	749.5	737.5	753.4	743.4
η_s	0.22	0.15	0.10	0.06
α (cm^{-1})	0.795	1.186	0.7231	0.8302
ESA Case	1	2	3	3
P_{thr} (W)	0.0364	0.0475	0.0439	0.0515
P_{int} (W)	-0.0083	-0.0099	-0.0067	-0.0071
σ_p (cm^2)	8.0×10^{-21}	11.8×10^{-21}	7.2×10^{-21}	8.3×10^{-21}
A		0.077		
B (W)		0.192		
C (W)			2.120	0.592
D (W^{-1})			0.0533	0.0545
f ($J^{-1}cm^{-2}$)		1.0×10^{27}	2.5×10^{26}	2.5×10^{26}
σ_5 (cm^2)	0	1.5×10^{-19}	0	0
σ_4 (cm^2)	0	0	5.2×10^{-20}	2.1×10^{-19}

Although fluorescence indicates that the brightest blue emission is due to ESA to $^4D_{3/2}$, the slope efficiencies have the greatest loss for ESA to $^2P_{3/2}$. The ESA cross sections obtained for the two processes are roughly equal (see Table VII). As described in a previous section, the difference in emission intensity is due to the higher emission cross sections associated with the spin allowed quartet-quartet transitions of $^4D_{3/2}$.

In summary, excited state absorption was proposed as the mechanism responsible for the losses in slope efficiency and increased laser threshold for alexandrite pumped Nd:BMAG. The losses due to excited state absorption and blue fluorescence are significant for high power alexandrite pumping and have been observed to reduce the slope efficiency by up to 73 % and elevate the threshold by up to 42 %. ESA to $^2P_{3/2}$ results in the greatest loss to the slope efficiency and the highest threshold. ESA to $^4D_{3/2}$ results in the greatest blue emission. The cross sections for the two ESA processes are approximately 2×10^{-19} cm^2. Initial attempts to lase the blue fluorescence proved unsucessful. Sample coating and optimization via excitation spectra may enable successful lasing in the blue in the future.

BIBLIOGRAPHY

1. Dieke, G. H., Spectra and Energy Levels of Rare Earth Ions in Crystals, (John Wiley and Sons, Inc., New York, 1968).

2. Allik, T. H., M. J. Ferry, R. J. Reeves, R. C. Powell, W. W. Hovis, D. P. Caffey, and R. Utano, to be published and presented at the annual OSA meeting, Orlando, FL (1989).

3. Weast, R. C. (editor),CRC Handbook of Chemistry and Physics 65^{th} edition, (CRC Press, Boca Raton, 1984) F-165.

4. Blasse, G., in Spectroscopy of Solid State Laser-Type Materials, edited by Baldassare Di Bartolo (Plenum Press, New York, 1987) p. 212.

5. Merkle, L. D. and R. C. Powell, Phys. Rev. B 20, 75.

6. Siegman, A. E., Lasers, (University Science Books, Mill Valley, 1986).

7. Forster, T., Ann. Phys. 2, 55 (1948).

8. Forster, T., Naturforsch 4, 321 (1949).

9. Forster, T., Discuss. Faraday Soc. 27, 7 (1959).

10. Inokuti, M. and F. Hirayama, J. Chem. Phys. 43, (1978).

11. Sardar, D., and R. C. Powell, J. Appl. Phys. 51, 2829 (1980).

12. Svelto, O., Principles of Lasers, (Plemum Press, New York, 1976).

13. Eisberg, R. and R. Resnick, Quantum Physics, (John Wiley and Sons, Inc., New York, 1974).

14. Kliewer, M. L., R. J. Reeves, and R. C. Powell, to be published.

VITA

MICHAEL JOHN FERRY

Candidate for the Degree of

Master of Science

Thesis: SPECTROSCOPIC AND LASER PROPERTIES OF Nd:BMAG

Major Field: Physics

Biographical:

Personal Data: Born in Frankfurt, West Germany, July 25, 1963, the son of Darwin and Margaret J. Ferry.

Education: Graduated from Patrick Henry High School, Roanoke, Virginia, in June, 1981; received Bachelor of Arts Degree from Wake Forest University in May 1985 with a major in physics; completed the requirements for the Master of Science Degree at Oklahoma State University in December, 1989.

Professional Experience: Graduate Research Assistant, Wake Forest University, May 1985 to August 1987; Graduate Teaching Assistant, Wake Forest University, September 1985 to August 1987; Summer Intern, Oak Ridge National Lab, May 1986 to August 1986; Graduate Teaching Assistant, Oklahoma State University, August 1987 to August 1988; Graduate Research Assistant, Oklahoma State University, August 1988 to present.